

1

2

3

4

Cosmic ray validation of electrode positions in small-strip thin gap chambers for the upgrade of the ATLAS detector

5

Lia Formenti

6

7

8

Department of Physics
McGill University, Montreal
October, 2021

9

10

11

12

13

A thesis submitted to
McGill University
in partial fulfillment of the
requirements of the degree of
Master of Science

¹⁵ Table of Contents

¹⁶	1	Introduction	1
¹⁷	2	High energy particle physics	4
¹⁸	2.1	The Standard Model	4
¹⁹	2.2	Beyond the Standard Model	6
²⁰	2.3	Studying high energy particle physics with accelerators	7
²¹	3	The LHC and the ATLAS experiment	9
²²	3.1	The Large Hadron Collider	9
²³	3.2	The High-Luminosity LHC	10
²⁴	3.3	The ATLAS experiment	12
²⁵	4	The New Small Wheels	18
²⁶	4.1	Motivation for the New Small Wheels	18
²⁷	4.2	Design of the NSWs	19
²⁸	4.3	Small-strip thin gap chambers	22
²⁹	4.4	sTGC Quadruplet Construction	25
³⁰	4.5	NSW alignment	26
³¹	5	Using cosmic muons to measure relative strip position offsets	30
³²	5.1	Cosmic rays	30
³³	5.2	Experimental setup	31

34	5.3 Data acquisition	31
35	5.4 Data preparation	33
36	5.4.1 Data quality cuts on electrode hits	33
37	5.4.2 Clustering and tracking	33
38	5.5 Relative local offsets	36
39	5.6 Systematic uncertainty	41
40	5.7 Discussion	42
41	6 Using x-rays to measure relative strip position offsets	44
42	6.1 Experimental setup	44
43	6.2 Data acquisition	46
44	6.3 Data preparation	46
45	6.4 Measuring local offsets	48
46	6.5 Measuring relative local offsets	48
47	7 Comparing cosmic muon and x-ray relative strip position offsets	52
48	7.1 Assessing correlation	52
49	7.2 Discussion	57
50	8 Outlook and summary	59
51	8.1 Outlook	59
52	8.2 Summary	60
53	References	61
54	APPENDICES	68
55	A Cluster position uncertainty	69
56	A.1 Cluster definition	69
57	A.2 Effect of fit algorithm on cluster mean	69
58	A.3 Effect of uncertainty in cluster mean on track residuals	70

59	B Analysis statistics	71
60	C Analysis systematics	73
61	C.1 Residual distribution fit function	73
62	C.2 Cosmic muon data collection voltage	74
63	C.3 Cluster fit algorithm	76
64	C.4 Differential non-linearity	77
65	D Printable plots	80

Abstract

67 The Large Hadron Collider (LHC) is used to generate subatomic physics processes at the
68 energy frontier to challenge our understanding of the Standard Model of particle physics.
69 The particle collision rate at the LHC will be increased up to seven times its design value in
70 2025-2027 by an extensive upgrade program. The innermost endcaps of the ATLAS muon
71 spectrometer consist of two wheels of muon detectors that must be replaced to maintain
72 the muon momentum resolution in the high-rate environment. The so-called New Small
73 Wheels (NSWs) are made of two detector technologies: micromegas and small-strip thin gap
74 chambers (sTGCs). The sTGCs are gas ionization chambers that hold a thin volume of gas
75 between two cathode boards. One board is segmented into copper readout strips of 3.2 mm
76 pitch that are used to precisely reconstruct the coordinate of a passing muon. Modules of
77 four sTGCs glued together into quadruplets cover the NSWs. Quadruplets were designed
78 to achieve a 1 mrad angular resolution to fulfill the spectrometer's triggering and precision
79 tracking requirements. To achieve the required angular resolution the absolute position of
80 the readout strips must be known in the ATLAS coordinate system to within 100 μm . At
81 McGill University, the performance of sTGC quadruplets was characterized using cosmic ray
82 data before being sent to CERN, where the charge profile left by x-rays is used to measure
83 the offset of the strip patterns with respect to nominal at a limited number of points on
84 the surface of each quadruplet. The x-ray strip position measurements have acceptable but
85 limited precision and do not span the whole area of the strip layers. Given the importance of
86 knowing the absolute position of each readout strip to achieve the performance requirements
87 of the NSWs, the x-ray method must be validated by an independent method. Cosmic ray
88 data is used to characterize the relative alignment between layers and validate the x-ray
89 method.

Résumé

Le grand collisionneur des hadrons (LHC) utilise des collisions de protons afin de générer des processus de la physique subatomique à la frontière même de la haute énergie, et ceci afin de tenter remettre en cause le modèle standard de la physique des particules. Le taux des collisions entre protons au LHC sera augmenté jusqu'à sept fois le taux nominal d'ici 2025-2027 à l'aide d'un programme de mise à niveau de grande envergure. Une partie du spectromètre à muons du détecteur ATLAS consistant de deux roues de détecteurs de muons doit être remplacée afin de maintenir la résolution sur l'inertie des muons à haut taux de collision. Appelées les Nouvelles Petites Roues (NSWs), elles utilisent deux technologies de détection différentes: des chambres micromegas et des chambres à petites bandes et à intervalles fins (sTGCs). Les sTGCs sont des chambres d'ionisation de gaz, qui contiennent un volume très fin de gaz entre deux panneaux cathodiques. Un panneau est segmenté avec de petites bandes en cuivre en pente de 3.2 mm. Ceux-ci détectent le signal et permettent la mesure précise des coordonnées spatiales des muons qui traversent le détecteur. Des modules de quatre sTGCs collés ensemble en quaduplets couvrent la superficie des NSWs. Ces quaduplets ont été conçus afin de permettre une résolution angulaire de 1 mrad, et de satisfaire les exigences des systèmes de déclenchement et de mesures de précision. Afin d'atteindre cette résolution angulaire il faut que la position absolue de chaque bande soit connue au sein du détecteur ATLAS avec une précision d'au moins 100 μm . À l'Université de McGill, la performance des quaduplets a été caractériser avec des rayons cosmiques avant leur envoi au CERN, où le profil des charges laissé par des rayons X est utilisé pour mesurer le déplacement du motif des bandes par rapport à leur emplacement nominal. Ceci est fait à un nombre de positions limité sur la surface des quaduplets. Ces déplacements, mesurés pas les rayons X, ont une précision acceptable mais limitée et ne couvrent pas la région entière des panneaux. Étant donné l'importance de la caractérisation précise de la position absolue de chaque bande afin de réaliser les exigences de rendement des NSWs, il faut une méthode indépendante de validation de la méthode des rayons X est requise. Les données recueillies avec les rayons cosmiques sont utilisées pour characteriser l'alignement relatif entre les panneaux et valider la méthode des rayons-X.

Acknowledgements

- 120 Experimental particle physics projects are never done alone. I am grateful to have been
121 working with the ATLAS Collaboration for two years now.
- 122 Thank you to Dr. Brigitte Vachon for her guidance throughout this project and for editing
123 this thesis. I am consistently amazed by her ability to jump into the details of my project
124 and discuss them with me.
- 125 Thanks also to Dr. Benoit Lefebvre, who collected some of the data used in this thesis, wrote
126 several software tools I used to analyze the data and advised me several times throughout
127 this project.
- 128 Thank you to my labmates at McGill University, Dr. Tony Kwan, Kathrin Brunner, John
129 McGowan and Charlie Chen. Kathrin taught me mechanical skills that I will apply elsewhere.
130 Tony, manager of the laboratory, created the most encouraging, trusting and productive work
131 environment I have ever been apart of.
- 132 Thank you to the friends I can call on at anytime, and thank you to my family whose
133 constant support makes every step possible.

Contribution of authors

I, the author, was involved in collecting the cosmic ray data from September 2019 - March 2021. I did not design the cosmic ray testing procedure nor write the data preparation software, but I participated in using the software to analyze cosmic ray results. In the thesis, the terms “clustering,” “local offset” and “relative local offset” are defined. Cosmic ray clustering was done in the data preparation software, but I redid the fit afterwards to explore sensitivity to the fit algorithm. With help from Dr. Lefebvre and Dr. Vachon, I helped design the software that calculated the relative local offsets from cosmic ray data. I wrote that software on my own. I was not involved in the design, data collection, data preparation or analysis of the x-ray data. I also was not involved in creating an alignment model from the x-ray data. I used the x-ray local offsets calculated using x-ray data analysis software to calculate relative local offsets with x-rays. I did the comparison between the x-ray and cosmic ray data.

I hereby declare that I am the sole author of this thesis. This is a true copy of the thesis, including any required final revisions, as accepted by my examiners.

₁₄₉

Chapter 1

₁₅₀

Introduction

₁₅₁ The Standard Model (SM) is a theoretical framework that describes experimental observa-
₁₅₂ tions of particles and their interactions at the smallest distance scales; however, the questions
₁₅₃ the SM does not address motivate more experimentation.

₁₅₄ Accelerators collide particles to generate interactions that can be recorded by detectors
₁₅₅ for further study. Detectors measure the trajectory and energy of all secondary particles
₁₅₆ produced in collisions to understand the interaction. The Large Hadron Collider (LHC) [1]
₁₅₇ at CERN is the world's most energetic particle accelerator. Its energy makes it a unique
₁₅₈ tool to study elementary particles and their interactions in an environment with conditions
₁₅₉ similar to what would have existed in the early universe. If study at the energy frontier is
₁₆₀ to continue, the LHC must go on.

₁₆₁ After 2025, the statistical gain in running the LHC further without significant increase in
₁₆₂ beam intensity will become marginal. The High Luminosity Large Hadron Collider (HL-
₁₆₃ LHC) project [2] is a series of upgrades to LHC infrastructure that will allow the LHC
₁₆₄ to collect approximately ten times more data than in the initial design by \sim 2030. The
₁₆₅ increase in LHC beam intensity will result in a large increase in collision rate that will make
₁₆₆ accessible and improve statistics on several measurements of interest [3], many only possible
₁₆₇ at the LHC and the energy frontier. The increase in beam intensity will also increase the
₁₆₈ level of background radiation, requiring major upgrades to the experiments used to record
₁₆₉ the outcomes of the particle collisions.

₁₇₀ The ATLAS experiment [4] is one of the LHC's general-purpose particle detector arrays, po-
₁₇₁ sitioned around one of the collision points of the LHC. During the 2019-2022 Long Shutdown
₁₇₂ of the LHC, the most complex upgrade of the ATLAS experiment is the replacement of the
₁₇₃ small wheels of the muon spectrometer with the so-called New Small Wheels (NSWs) [5].

174 The detector upgrade addresses both the expected decrease in hit efficiency of the precision
175 tracking detectors and the high fake trigger rate expected in the muon spectrometer at the
176 HL-LHC. The NSWs are made of two different detector technologies: micromegas and small-
177 strip thin gap chambers (sTGCs). Micromegas are optimized for precision tracking while
178 sTGCs are optimized for rapid triggering, although each will provide complete coverage and
179 measurement redundancy over the area of the NSWs. Eight layers each of sTGCs cover the
180 NSWs. Practically, countries involved in detector constructor created quadruplet modules of
181 four sTGCs glued together that were arranged and installed over the area of the NSWs once
182 they arrived at CERN. Teams across three Canadian institutions built and characterized 1/4
183 of all the required sTGCs.

184 The sTGCs are gas ionization chambers that consist of a thin volume of gas held between two
185 cathode boards. One board is segmented into strip readout electrodes of 3.2 mm pitch. The
186 position of the particle track in the precision coordinate can be reconstructed from the strip
187 signals [5]. The sTGCs achieved the design track spatial resolution in the precision coordinate
188 of less than 100 μm per detector plane that will allow them to achieve a 1 mrad track angular
189 resolution using the 8 layers of sTGC on the NSW [6, 5]. The NSW measurement of the
190 muon track angle will be provided to the ATLAS trigger and used to reject tracks that do
191 not originate from the interaction point [5].

192 The precise measurement of a muon track angle depends on knowing the position of each
193 readout strip within the ATLAS coordinate system. To achieve this, the position of specific
194 locations on the surface of sTGC quadruplets will be monitored by the ATLAS alignment
195 system to account for time-dependent deformations [5]. Within a quadruplet module, the
196 strip positions could have been shifted off of nominal by non-conformities of the strip pattern
197 etched onto each cathode boards [7] and shifts between strip layers while gluing sTGCs into
198 quadruplets.

199 An x-ray gun was used to measure the offset of strips from their nominal position at the
200 locations that will be monitored by the ATLAS alignment system thereby providing, locally,
201 an absolute “as-built” strip position within the ATLAS coordinate system. Estimates of the
202 “as-built” positions of every readout strip are obtained by building an alignment model from
203 the available x-ray measurements [8].

204 The technique of measuring the “as-built” strip positions using x-ray data has never been
205 used before and must be validated. This thesis describes the use of cosmic muon data,
206 recorded to characterize the performance of each Canadian-made sTGC module, to validate
207 the x-ray strip position measurements. A description of how this work fits within the overall
208 alignment scheme of the NSW is also presented.

209 *Rewrite after implementing Brigitte’s edits.* Chapters 3 and 4 give more background on
210 particle physics, the LHC, ATLAS, the NSWs, and sTGCs. In chapter 5, the cosmic ray

211 testing procedure and how the position of the strips can be probed with cosmics data is
212 presented. Chapter 6 introduces the x-ray method, and in chapter 7, the x-ray offsets are
213 validated with cosmic muon data. The thesis concludes with a summary and outlook in
214 chapter 8.

215 **Chapter 2**

216 **High energy particle physics**

- 217 Particle physics aims to study the elementary constituents of matter. Understanding the fundamental building blocks and how they interact provides insight into how the early universe evolved to the forms of matter we observe today. This chapter introduces general concepts in particle physics relevant to understanding the physics goals of the High-Luminosity LHC (HL-LHC) and NSWs upgrade.
- 222 The information on particle physics and the SM presented here is rather general; the interested reader is referred to [9, 10, 11] for more information.

224 **2.1 The Standard Model**

- 225 The Standard Model (SM) is a theoretical framework developed in the early 1970's that describes the observed elementary particles and their interactions. It is built on a collection of quantum field theories and has been remarkably successful at predicting experimental observations, including but not limited to the existence of the top quark [12], the tau neutrino [13] and the Higgs boson [14, 15].
- 230 The known elementary particles described by the SM are represented in figure 2.1. There are 12 matter particles (six quarks and six leptons), 4 force-mediating particles, and the Higgs boson. Each matter particle also has an anti-matter particle pair with the same mass but opposite charge, not represented in figure 2.1. The different forces of nature are understood to be the result of the exchange of force-mediating particles between interacting (coupled) particles. Photons are mediators of the electromagnetic force, W⁺/- and Z bosons are mediators of the weak force, and gluons are mediators of the strong force. At high

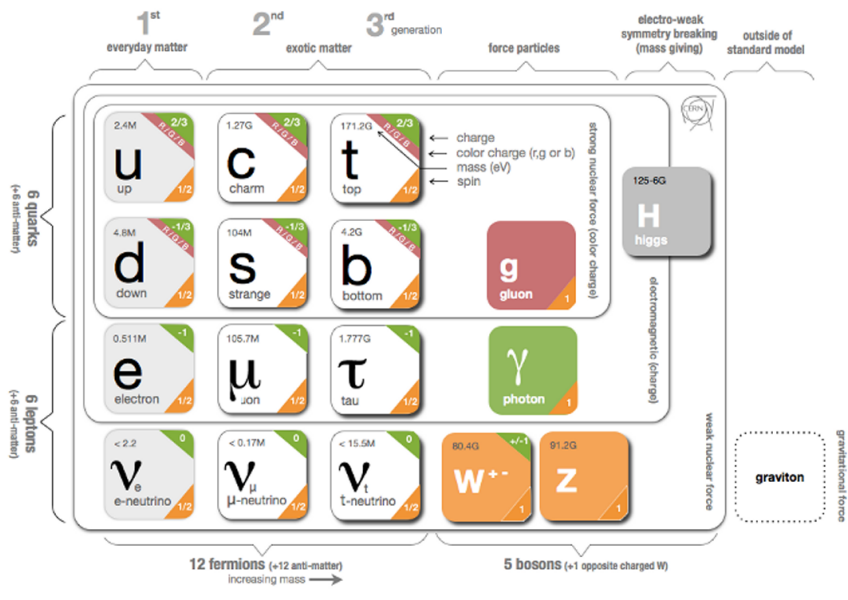


Figure 2.1: Schematic diagram of all elementary particles in the SM. Particles are grouped according to their properties and the forces through which they interact with other particles [16].

237 energy, the SM describes the electromagnetic and weak forces as stemming from a unified
238 electroweak force. The Higgs boson field interacts with the particles mediating the unified
239 electroweak force to distinguish the weak and electromagnetic forces from each other at lower
240 energies and give particles (except neutrinos) a mass. This is called electroweak symmetry
241 breaking.

242 Quarks are matter particles that are sensitive to all forces; notably they are the only particles
243 sensitive to the strong force. Protons and neutrons are made up of quarks and gluons, and the
244 strong force is responsible for their existence and mutual attraction into nuclei [17]. Leptons
245 are particles not sensitive to the strong force. Charged leptons include the electron, which
246 once part of atoms is responsible for chemistry. Of particular importance for this thesis is
247 the charged lepton called a muon. It is like the electron but its mass is \sim 200 times larger
248 than that of the electron. Muons have a lifetime of $2.2\ \mu\text{s}$ [11] and decay predominantly as
249 $\mu \rightarrow e^-\bar{\nu}_e\nu_\mu$. Neutrinos are neutral, almost massless leptons that only interact through the
250 weak force.

251 Common matter is made up of the lightest constituents of the SM: up and down quarks,
252 electrons and photons. The other particles are produced in high-energy environments but
253 then decay to the lightest constituents. Such high energy environments include the condi-
254 tions present in the early universe [18], astrophysical sources, and particle accelerators. The
255 presence of the particles of the SM at the beginning of the Universe means that their inter-
256 actions and decays are fundamental for the study of the evolution of the early universe [18].
257 Many high energy astrophysical sources, like supernovae, generate particles that rain down
258 on Earth as cosmic rays [19]. Particle accelerators have been built to create controlled en-
259 vironments of high-rate, high-energy particle collisions at high energy where the production
260 and decay of elementary particles can be directly studied.

261 2.2 Beyond the Standard Model

262 Despite its success at describing most experimental observations to date, there is ample
263 evidence that the SM is not a complete description of natural phenomena at the smallest
264 scales. For example, the SM has a large number of free parameters, the values of which have
265 to be fine-tuned to fit experimental observations. This is part of the so-called “naturalness”
266 problem.

267 Furthermore, the SM provides no explanation for several open questions in particle physics.
268 First, neutrinos in the SM are assumed to be massless and do not gain mass in the same way
269 as the other particles. However, neutrino were confirmed to change between their different
270 flavours in 2013 [20], which can only occur if neutrinos do have mass [21]. The neutrino

271 mass requires physics beyond the standard model [22]. Second, several astrophysical and
272 cosmological measurements suggest the presence of “dark matter” making up 85 % of the
273 matter content of the universe [23]. The nature of dark matter is unknown and so far there
274 is no SM explanation [24]. Third, the SM does not explain the origin and nature of the
275 matter-antimatter asymmetry that produced our matter-dominated universe. Finally, the
276 SM does not include a description of gravity.

277 Theoretical extensions beyond the Standard Model (BSM) aim to address some of these
278 questions, often predicting existence of yet-unseen elementary particles or physics phenomena
279 beyond those predicted by the SM. These hypothetical new physics phenomena or new
280 particles can be searched for at particle accelerators.

281 **2.3 Studying high energy particle physics with acceler- 282 erators**

283 In particular, particle accelerators of increasingly higher energy have a long history of en-
284 abling the discovery of predicted particles. These include, for example, the discovery of
285 the W [25, 26] and Z bosons [27, 28], the top quark [29, 30], and most recently, the Higgs
286 boson [31, 32]. The discovery of the Higgs boson marked the completion of the SM as it is
287 known today.

288 Based on the established success of the SM, there are two approaches to particle physics
289 research. One approach is to search for the existence of new physics phenomena predicted
290 to exist in BSM theories and the other is to test the validity of the SM to a high degree of
291 accuracy to search for flaws in the model. Standard Model predictions are generally expressed
292 in terms of the probability of a specific physics process to occur, expressed as a cross section
293 in units of barns (with 1 barn = 10^{-28} m²). As an example, figure 2.1 shows a summary
294 of cross section measured for different physics processes using the ATLAS experiment and
295 their comparison with the predictions of the SM. Most cross section measurements agree
296 well within one standard deviation with the SM predictions.

297 Particle accelerators provide a controlled and high-collision rate environment that makes
298 them ideal places to search for new physics phenomena and to carry out systematic tests of
299 the SM. The LHC is the highest energy collider in the world so it can access physics that
300 no other accelerator can. A description of the LHC and the ATLAS detector are provided
301 in the next chapter.

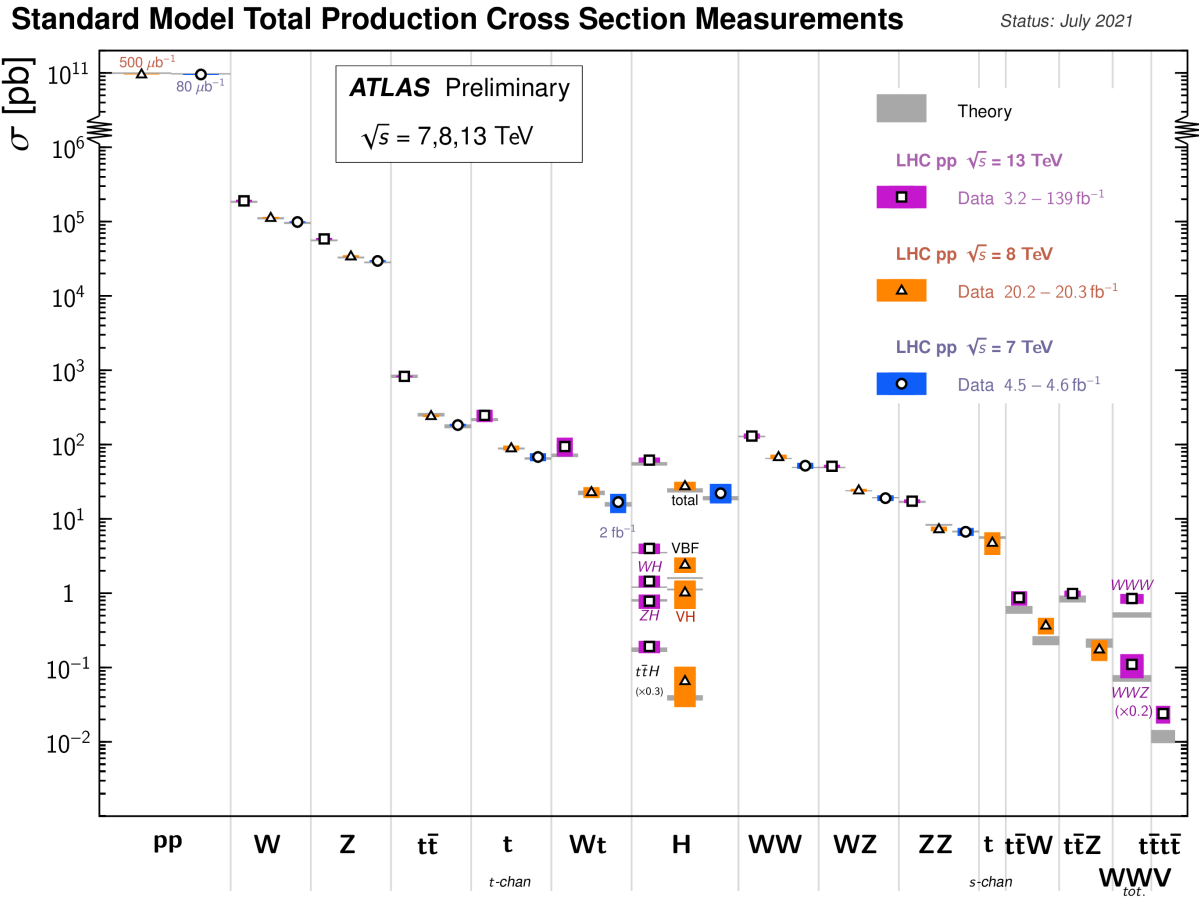


Figure 2.2: Production cross sections of different final states measured by the ATLAS experiment at the LHC. Comparison with the SM theory predictions is also shown [33].

302 **Chapter 3**

303 **The LHC and the ATLAS experiment**

304 The Large Hadron Collider (LHC) is the world's most energetic particle accelerator and the
305 ATLAS experiment is used to record the results of particle collisions at the LHC. In this
306 chapter, details about both that are necessary to understand the High-Luminosity LHC (HL-
307 LHC) upgrade project and the ATLAS experiment's New Small Wheels (NSWs) upgrade
308 are presented.

309 **3.1 The Large Hadron Collider**

310 The LHC is an accelerator 27 km in circumference and located \sim 100 m underground at
311 the CERN laboratory near Geneva, Switzerland [1]. It has two beam pipes within which
312 bunches of protons counter-circulate before being collided in the center of one of four major
313 experiments, such as the ATLAS experiment (discussed in section 3.3). Protons are guided on
314 the circular trajectory using 1232 superconducting dipole magnets capable of a maximum
315 field of 8.33 T. Radio-frequency accelerating cavities are used to accelerate protons to a
316 the maximum design energy of 7 TeV [34]. During LHC Run-1 (2011-2012), protons were
317 collided at a collision center-of-mass energy of 7 TeV and 8 TeV [35]. During LHC Run-2
318 (2015-2018), the center-of-mass energy of proton collisions was increased to 13 TeV [36],
319 close to the maximum design value of 14 TeV [34]. It is not actually the protons that
320 interact, but the constituent quarks and gluons that each carry some fraction of the energy
321 and momentum of the collisions.

322 **Luminosity**

323 The number of proton-proton interactions generated by the LHC directly affects the statistics

available to make measurements of interaction cross sections. Predicting the number of proton-proton interactions requires defining a metric called luminosity [11]. The luminosity of a particle collider is the number of particles an accelerator can send through a given area per unit time. It is calculated from the measurable quantities in Equation 3.1:

$$\mathcal{L} = \frac{f N_1 N_2}{4\pi\sigma_x\sigma_y}, \quad (3.1)$$

where f is the frequency of the bunch crossings (25 ns), N_1 and N_2 are the number of protons in each bunch ($\sim 10^{11}$ protons / bunch), and σ_x and σ_y are the RMS of the spatial distributions of the bunch. Therefore, luminosity is a property of accelerator beams, which are set by the capabilities of the accelerator. The design luminosity of the LHC was $10^{34} \text{ cm}^{-2}\text{s}^{-1}$. The units of luminosity are an inverse area; multiplying the luminosity by the cross section of a given process gives the expected rate for that process.

Integrating the *instantaneous* luminosity (equation 3.1) over a period of data collection time gives the integrated luminosity,

$$L = \int \mathcal{L}(t) dt \quad (3.2)$$

which is related to the total number of interactions. In this way, the luminosity is the link between the accelerator and the statistical power of measurements to be made with the data collected. So far, the LHC provided an integrated luminosity of 28.26 fb^{-1} in Run-1 [35] and 156 fb^{-1} in Run-2 [36].

3.2 The High-Luminosity LHC

At the end of the LHC program in 2025, the statistical gain on measurements in running the LHC further will become marginal. The HL-LHC [2] project consists of the upgrade of LHC infrastructure to achieve a nearly ten fold increase in instantaneous luminosity, thereby improving measurement statistics as well. Also, some systems will need repair and replacement to operate past ~ 2020 . The LHC will continue to be the most energetic accelerator in the world for years to come and is the only accelerator with enough energy to directly produce the Higgs boson and top quarks. Therefore, the European Strategy for Particle Physics made it a priority “to fully exploit the physics potential of the LHC” with “a major luminosity upgrade” [37]. The goal is for the HL-LHC to provide an integrated luminosity of 3000 fb^{-1} in the 12 years following the upgrade. The luminosity actually



Figure 3.1: The LHC/HL-LHC timeline [38]. The integrated luminosities collected and projected for each run of the LHC are shown in blue boxes below the timeline and the center of mass energy of the collisions is shown in red above the timeline. The top blue arrow labels the run number. The acronym “LS” stands for “long shutdown” and indicates periods where the accelerator is not operating. During the shutdowns, upgrades to the LHC and the experiments are taking place. This timeline was last updated in January, 2021, and reflects changes in the schedule due to the ongoing pandemic.

351 achieved will depend on a combination of technological advances and upgrades in progress
 352 that affect the factors contributing to luminosity defined in equation 3.1 [2]. Figure 3.1 shows
 353 the projected schedule of the HL-LHC upgrades and operation [38].

354 One of the most anticipated measurements at the HL-LHC is the value of the triple-Higgs
 355 coupling. Measuring the coupling will allow the determination of the shape of the Higgs
 356 potential responsible for electroweak symmetry breaking. Any discrepancy with respect to
 357 the SM prediction will show that there must be other sources of electroweak symmetry
 358 breaking, and hence physics phenomena beyond the SM. The LHC is the only accelerator
 359 where the Higgs boson can be produced directly so it is the only place where the triple-Higgs
 360 coupling could be measured. The HL-LHC upgrade is required to produce a significant
 361 sample of Higgs produced in pairs to make a statistically meaningful measurement [3, 39].

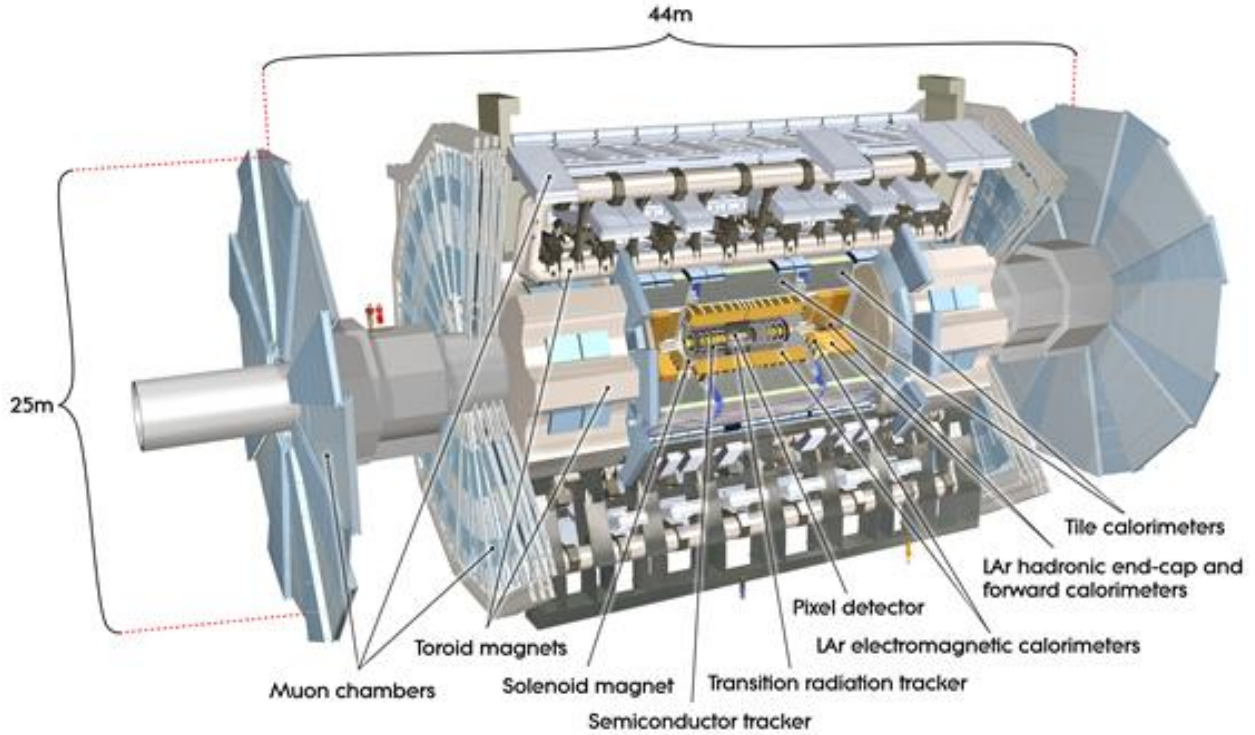


Figure 3.2: Schematic diagram of the ATLAS experiment, with the various detector subsystems labelled [4].

362 Accordingly, detector sensitivity to various Higgs decays will be important at the HL-LHC.

363 3.3 The ATLAS experiment

364 The ATLAS experiment [4] was designed to support all the physics goals of the LHC. It
365 is 44 m long and 25 m in diameter, and weighs 7000 tonnes. The ATLAS experiment is
366 centered around one of the LHC's interaction points (a place where the beams collide). As
367 shown schematically in figure 3.2, ATLAS consists of an array of particle detector subsystems
368 arranged concentrically around the beam pipe. The ATLAS experiment is cylindrical because
369 it aims to provide 4π coverage around the interaction point. In reference to the cylindrical
370 geometry of the experiment, it is helpful to separate the subsystems of ATLAS into the
371 so-called "barrel" and "endcap"/"forward" regions.

372 For analysis purposes, a spherical coordinate system is defined. The azimuthal angle ϕ is
373 measured around the beampipe and the polar angle θ is measured from the beam pipe. The
374 polar angle is more often expressed in terms of pseudo-rapidity, defined as $\eta = -\ln \tan(\theta/2)$.
375 Pseudo-rapidity values vary from 0 (perpendicular to the beam) to $\pm\infty$ (parallel to the
376 beam, defined as the z-direction) and is an approximation to the rapidity of a particle when
377 its momentum is much greater than its mass. It is useful to describe the direction of outgoing
378 particles in proton-proton collisions because differences in rapidity are invariant to a Lorentz
379 boost along the beam direction.

380 The ATLAS experiment provides identification and kinematic measurements for each particle
381 created after the initial collision, which is done by assembling offline the information recorded
382 by each subsystem. With this information, signatures of processes of interest can be identified
383 and studied. An overview of the main ATLAS subsystems is given below.

384 **The inner detector**

385 The inner detector [40, 41] (figure 3.3) is for precise measurements of charged particle tra-
386 jectories, measurement of primary and secondary interaction vertices and assistance in the
387 identification of electrons. A 2 T solenoid with field parallel to the beam bends the trajec-
388 tory of outgoing charged particles. A measurement of the bending radius of each charged
389 particle provides information about its momentum. The innermost part of the inner tracker
390 is made of high-resolution semiconductor pixel and strip detectors while the outermost part
391 is made of straw-tubes. The straw tubes are used in the trajectory measurements but they
392 are also interspersed with material designed to enhance the creation of transition radiation.
393 Transition radiation occurs when a highly relativistic charged particle traverses a material
394 boundary [42]. The amount of transition radiation emitted by a charged particle is detected
395 by the straw-tubes and is used to identify electrons.

396 **Calorimetry system**

397 Electromagnetic and hadronic sampling calorimeter units are used to record the energy
398 of electrons, photons and jets¹. A combination of liquid-argon (LAr) electromagnetic and
399 hadronic calorimeters [43] and tile-scintillator hadronic calorimeters [44] cover the rapidity
400 range $|\eta| < 4.9$, as shown in figure 3.4.

401 Sampling calorimeters have alternating layers of dense material and material that can mea-
402 sure the amount of ionization by charged particles. The dense material causes incoming

¹When quarks or gluons are expelled in a high energy collision, they create collimated groups of hadrons because they carry a charge called “colour”, and nature only allows “colourless” combinations to exist [42].

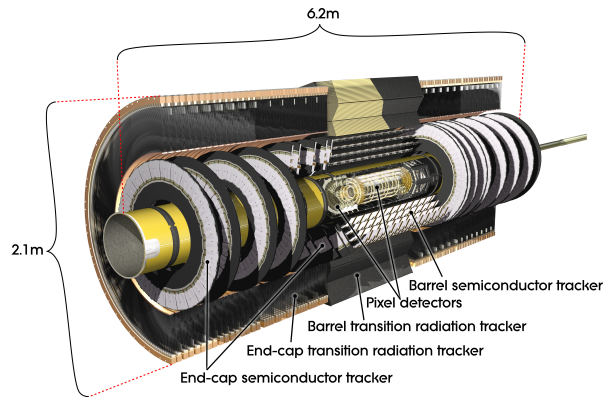


Figure 3.3: Schematic diagram of the ATLAS experiment's inner detector, with the different segments and the technology used labeled [4].

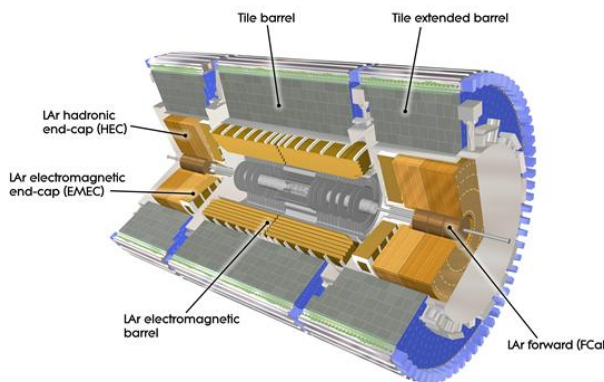


Figure 3.4: Schematic diagram of the ATLAS calorimeter system, with the different segments and the technology used labeled [4].

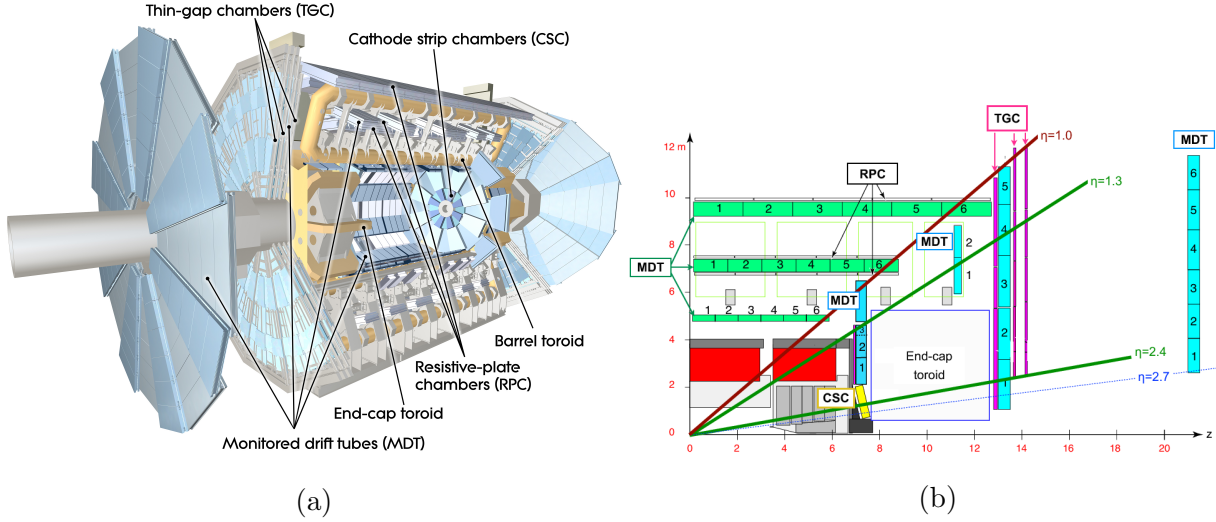


Figure 3.5: Schematic diagram of the ATLAS muon spectrometer. Figure (a) shows a 3D projection of the system with the different types of chambers and different parts of the toroidal magnet system labeled [4]. Figure (b) shows a projection of one quarter of the muon spectrometer, with the interaction point in the bottom left corner. The small wheel is just left of the end cap toroid, the big wheel is to its right, and the outer wheel is the rightmost structure [47].

403 charged particles to shower into lower energy particles and deposit their energy in the sen-
 404 sitive volume. Only muons and neutrinos are known to pass the calorimeters to the muon
 405 spectrometer without being absorbed.

406 Muon spectrometer

407 The muon spectrometer [45] consists of multiple layers of tracking chambers embedded in
 408 a 2 T magnetic field generated by an air-core superconducting toroid magnet system. Fig-
 409 ure 3.5a shows a schematic diagram of the layout of the different chambers and of the toroid
 410 magnets [4]. The trajectory of a muon is reconstructed from the information recorded by
 411 the different types and layers of tracking chambers. The amount of bending in the magnetic
 412 field provides a measure of the muon's momentum. In the barrel section of ATLAS, the
 413 toroidal magnetic field is created by eight coils bent into the shape of a "race-track" and
 414 symmetrically arranged around the beampipe. In the forward region, two end-cap toroids,
 415 each with eight smaller racetrack-shaped coils arranged symmetrically around the beam pipe
 416 are inserted in the ends of the barrel toroid [46].

417 The muon spectrometer is separated into detectors used for precision offline tracking and

418 for triggering purposes. Three layers of monitored drift tubes (MDTs) or cathode strip
419 chambers (CSCs) are used for tracking. The position of the muon track in each of the three
420 layers allows reconstruction of the bent trajectory of a muon and hence its momentum. To
421 satisfy the muon spectrometer target momentum resolution of $\Delta p_T/p_T < 1 \times 10^{-4}$ p / GeV
422 for $p_T < 300$ GeV and a few percent for lower p_T muons, the MDTs and CSCs were designed
423 to achieve a spatial resolution of 50 μm each. Accordingly, an optical alignment system was
424 designed to monitor and correct for chamber positions [45, 48].

425 Resistive plate chambers (RPCs) are used for triggering in the barrel and thin-gap chambers
426 (TGCs) are used for triggering in the endcaps. The positions of each type of chamber
427 are sketched in figure 3.5b. The endcap section of the muon spectrometer consists of three
428 sections, the small wheel, big wheel, and outer wheel – ordered by proximity to the interaction
429 point. In Run-1, low (high) p_T muons were triggered on if two (three) of the RPC or TGC
430 layers around the big wheel fired in coincidence, for the barrel and endcaps respectively [49].
431 After Run-1 it was discovered that up to 90% of the triggers in the endcap were fake, caused
432 by background particles generated in the material between the small wheel and the big
433 wheel [5]. To reduce the fake rate in Run-2, the TGCs on the inside of the small wheel also
434 had to register a hit. The added condition reduced the trigger rate by 50% in the range $1.3 < |\eta| < 1.9$ [50]. The effectiveness of the solution was limited since the $|\eta|$ -range of the small
436 wheel TGCs was limited to $1.0 < |\eta| < 1.9$ and the spatial resolution of the small wheel
437 TGCs is coarse [5].

438 Trigger system

439 It would be impossible to record all the data from bunch crossings every 25 ns, corresponding
440 to a rate of ~ 40 MHz. The ATLAS experiment has a multi-level trigger system to select
441 events of interest for permanent storage. The Level-1 (L1) hardware trigger [49] uses partial-
442 granularity information from the muon spectrometer and calorimeters to trigger on high p_T
443 muons, electrons, jets, missing transverse energy, and τ decaying to hadrons. After Run-3
444 an upgrade of the trigger system will allow a maximum trigger rate of 1 MHz with a latency
445 of 10 μs [51], but for now the working limits are a rate of 100 kHz [50] and 2.5 μs [49].

446 The L1 trigger is used to define regions of interest that are fed into the software high level
447 trigger (HLT) [52], in which the full granularity of the muon spectrometer and calorimeter
448 are used with information from the inner detector to reduce the trigger rate to 1 kHz. Events
449 that satisfy at least one of the L1 and HLT trigger criteria are recorded to permanent storage
450 for offline analysis.

452 With the foreseen increase in luminosity at HL-LHC, it is a priority to upgrade the ATLAS
453 detector to further reduce the muon trigger fake rate in the forward region. The New Small
454 Wheels being commissioned to replace the original ATLAS muon small wheels will address
455 this challenge.

456 **Chapter 4**

457 **The New Small Wheels**

458 **4.1 Motivation for the New Small Wheels**

459 The hit rate of all detector systems will significantly increase during HL-LHC operation
460 because of the increase in luminosity. The increased rate presents a challenge for both the
461 tracking and triggering capabilities of the muon spectrometer [5].

462 In terms of precision tracking, the maximum hit rate in the MDTs is expected to reach above
463 300 kHz by the end LHC operation. At this rate, the hit efficiency of MDTs decreases by
464 35%, mostly due to the long dead-time of the chambers. Losing hits in the small wheel will
465 reduce the high p_T muon momentum resolution. The decrease in resolution will affect the
466 ability to search for, for example, the decay of hypothetical heavy bosons (W' , Z') or other
467 hypothetical particles beyond the SM [3].

468 Already during LHC Run-2 operation, the forward muon trigger system had to cope with a
469 very high fake rate, even with the inclusion of TGC data from the small wheel as part of the
470 trigger criteria. At the luminosity expected in Run-3, it is estimated that 60 kHz out of the
471 maximum L1 trigger bandwidth of 100 kHz would be taken up by forward muon triggers.
472 To address this challenge, a possible solution would be to raise the minimum p_T threshold
473 from 20 GeV to 40 GeV. However, this would have an adverse impact on the ability to study
474 several physics processes of interest that depend on low p_T muons, particularly the Higgs
475 decay to two muons, the Higgs decay to two tau leptons and hypothetical particle decays
476 beyond the SM [5].

477 The NSWs will address both of these problems. They will be made of precision tracking
478 chambers suitable for the expected hit rates during the HL-LHC and triggering chambers
479 capable of 1 mrad track angular resolution. The idea behind the design triggering capability

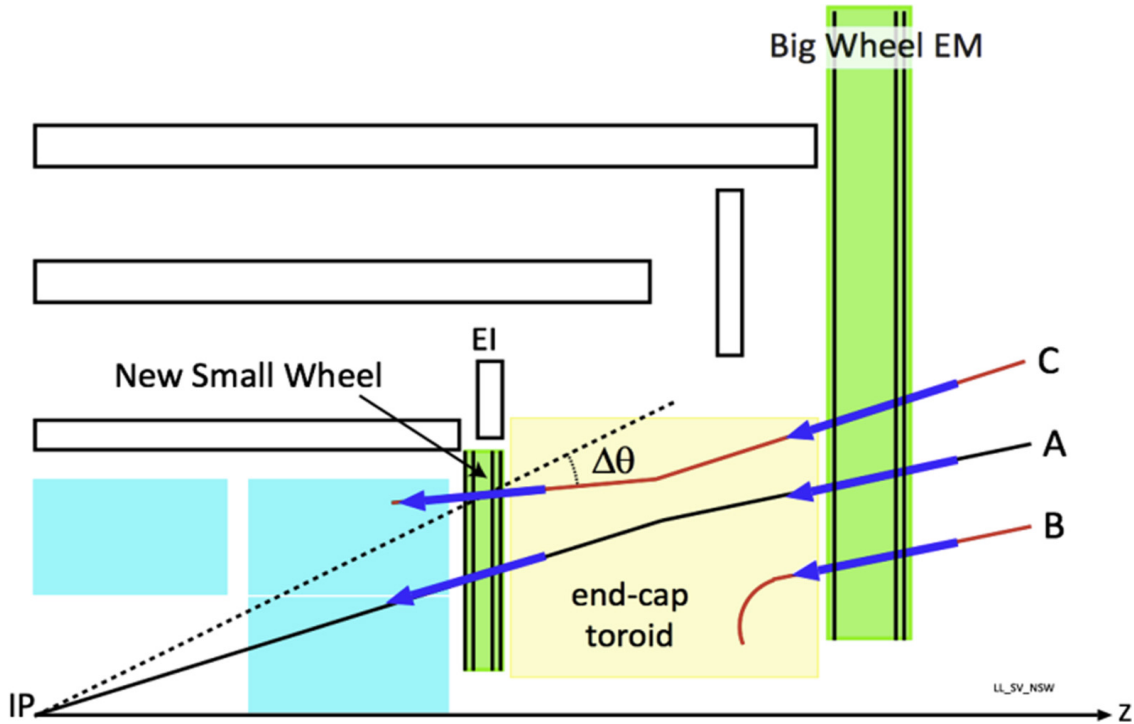


Figure 4.1: A schematic diagram of a quarter cross section of the ATLAS muon spectrometer, with the interaction point (IP) in the bottom left corner. Three possible tracks are labeled. Ideally, track A would be triggered on while track B and C discarded. With the old small wheel, all three tracks would be recorded. With the NSW, only track A would be recorded [5].

of the chambers is to allow matching of track segments measured by the NSW with track segments from the big wheel to discard tracks not originating from the interaction point. Figure 4.1 illustrates this point: the Run-2 trigger system would have triggered on all three tracks (A, B, C) while with the NSW the trigger system would only trigger on track A. The NSWs will therefore make it possible to maintain a low muon p_T trigger threshold and maintain an adequate muon momentum resolution during HL-LHC operations, which will allow the full exploitation of the physics potential of this research program [5].

4.2 Design of the NSWs

The NSWs are made with two detector technologies: micromegas and small-strip thin gap chambers. Eight layers of each cover the entire area of the wheel. Micromegas are designed

490 to be the primary precision tracking detectors and sTGCs the primary triggering detectors,
491 but both technologies offer full redundancy by being capable of providing both precision
492 measurements and trigger information. Both types of detectors were designed to achieve
493 spatial resolution better than $\sim 100 \mu\text{m}$ per layer. Four chambers are glued together to create
494 quadruplet modules of each detector type. Quadruplets of different sizes, most shaped as
495 trapezoids, are assembled into wedges. Two sTGC wedges and two micromegas wedges are
496 layered to create sectors (with the sTGC wedges on the outside) [5]. Different stages of the
497 construction process are shown in figure 4.2. At the time of writing, the assembly of the
498 NSWs has just been completed. The first NSW has been lowered into the ATLAS cavern
499 and is being commissioned and the second will be lowered shortly.



(a) A sTGC quadruplet module. The left image highlights the trapezoidal shape of a quadruplet module. The right image shows the corner at the short edge, where the four sTGC layers and each layer's gas inlet are visible. The gas outlets and high voltage cables are located along the long edge near the corner in the back left of the photo. The green printed circuit board along the sides are the adaptor boards where the front end electronics are attached.



(b) Left: A sTGC wedge. The white frame outlines the individual quadruplet modules that have been glued together into a wedge. Right: A completed sector, with two sTGC wedges on the outside and two micromegas wedges on the inside.



(c) A picture of one of the two NSWs. All sectors except one large sector at the top are installed, revealing two of the smaller sectors that are normally hidden under the large sectors and support bars. The NSWs are 9.3 m in diameter.

Figure 4.2: Images showing different stages of NSW construction.

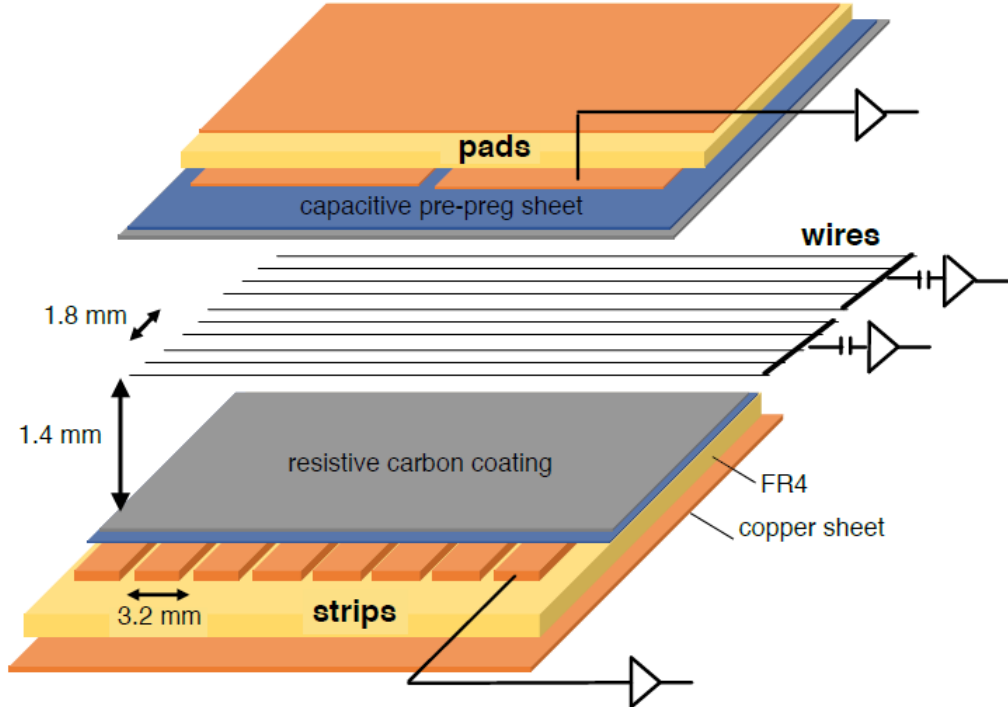


Figure 4.3: Internal structure of an sTGC, zoomed into the area under a pad. High voltage is applied to wires suspended in the gas volume to create an electric field. A passing muon causes an ionization avalanche that is picked up by the wire, strip and pad electrodes [8].

500 4.3 Small-strip thin gap chambers

501 The sTGCs are gas ionization chambers operated with a gas mixture of CO₂:n-pentane with
 502 a ratio of 55%:45% by volume. Gold-plated tungsten wires, 50 µm in diameter and with
 503 1.8 mm pitch, are suspended between two cathode planes made of FR-4, each 1.4 mm away
 504 (see figure 4.3). One cathode board is segmented into copper pads of varying area (with a
 505 typical size of $\sim 300 \text{ cm}^2$ each), and the other is segmented into copper strips of 3.2 mm pitch
 506 running lengthwise perpendicular to the wires. High voltage is applied to the wires and the
 507 cathode planes are grounded [5, 53]. When a muon passes through a sTGC, it will ionize some
 508 of the atoms in the gas and the electric field in the gas gap will result in the formation of an
 509 ionization avalanche [54]. The motion of the ions and free electrons generates small currents
 510 on the nearby wire and capacitatively-coupled strip and pad electrodes [5]. The gas mixture

511 was chosen to absorb excess photons produced in the avalanche that delocalize the avalanche
512 signal [55] and saturate many strip electrodes, preventing the formation of streamers [42].
513 This allows the chambers to be run at a higher high-voltage providing a faster response and
514 higher signal [55] . The resistivity of the carbon coating and capacitance of the pre-preg
515 sheet tune the spread of the charge distribution [56] and the speed of the response [57] to
516 optimize the rate capability. The combined information from the strip readout electrodes
517 and wires provide the location where the muon passed through the chamber. The small pitch
518 of the strip readout electrodes is what allows the quadruplets to deliver good track angular
519 resolution to improve the fake trigger rate and meet the precision tracking requirements [5].

520 A 3-out-of-4 coincidence in pad electrodes from each layer of a quadruplet defines a region of
521 interest where the strip and wire electrodes should be read out. The pad triggering scheme
522 greatly reduces the number of electrodes that require readout so that a track segment of the
523 required angular resolution can be provided quickly enough to the hardware trigger [5].

524 Signal is read out from groups of successive wires, so the position resolution in the direction
525 perpendicular to the wires is 10 mm per plane. The wires give the azimuthal coordinate
526 in ATLAS so the position resolution in this direction is sufficient. Good resolution on the
527 η coordinate, perpendicular to the strips, is important [5]. In a test beam environment,
528 the strip spatial resolution of a single sTGC was measured to be 45 microns for muon
529 perpendicularly incident on the surface of the sTGC. Although the spatial resolution worsens
530 as function of muon angle measured from normal incidence [58], when four sTGCs are glued
531 together into a quadruplet the design angular resolution of 1 mrad in the strip coordinate is
532 achievable [5, 53].

533 To achieve the required track angular resolution once installed in ATLAS, the absolute
534 position of each sTGC strip within the ATLAS coordinate system must be accurately known.
535 The degree of accuracy required is on the order of the position resolution of the chambers,
536 $\sim 100 \mu\text{m}$. The NSW alignment system, detailed in section 4.5, will monitor the position of
537 alignment platforms installed on the surface of the wedges. The alignment platforms are
538 installed with respect to an external reference on the sTGCs: two brass inserts on each strip
539 layer on one of the angled sides of each quadruplet (shown in figure 4.4). So the challenge
540 of monitoring the position of the strips in ATLAS was separated into two steps: first, infer
541 the position of the strips with respect to the brass inserts using the sTGC design geometry;
542 second, use the alignment system to monitor the position of the alignment platforms. The
543 next section provides some pertinent details on the sTGC construction process, with steps
544 that affect the position of the strips with respect to the brass inserts highlighted.



(a) Brass insert near long edge.

(b) Brass insert near short edge.

Figure 4.4: The brass inserts sticking out from the gas volumes of an sTGC quadruplet. These inserts were pressed against alignment pins when the individual sTGCs were being glued together.

545 4.4 sTGC Quadruplet Construction

546 Five countries were responsible for producing sTGC quadruplets of varying geometries for the
547 NSW: Canada, Chile, China, Israel and Russia. Canada was responsible for the construction
548 of one quarter of the required sTGCs, of three different quadruplet geometries. The steps of
549 the construction process in each country were similar [5]. The process followed in Canada is
550 detailed here.

551 A research group at TRIUMF in Vancouver, British Columbia was responsible for preparing
552 the cathode boards. The boards were made and the electrodes etched on at a commercial
553 laboratory, Triangle Labs, in Carson City, Nevada. Once completed they were sent to TRI-
554 UMF to be sprayed with graphite and to have support structures glued on [7]. The boards
555 are commercial multilayer printed circuit boards, but the strip boards required precision ma-
556 chining to etch the strip pattern [5]. Triangle Labs also machined the two brass inserts into
557 each strip board. A coordinate measuring machine (CMM) was used to accurately measure
558 the position of a set of reference strips on each board. Four quality parameters describing
559 non-conformities in the strip pattern of each board with respect to the brass inserts were
560 derived from the data and the results are available on a QA/QC database. The parameters –
561 offset, angle, scale and nonparallelism – and the CMM data collection is described in full
562 in [7]. Due to time constraints, tolerances on the non-conformities in the etched strip pattern
563 with respect to the brass inserts were loosened, with the condition that the strip positions
564 in ATLAS would have to be corrected for [7].

565 The prepared boards were sent to Carleton University in Ottawa, Ontario for construction
566 into sTGCs and quadruplets. First, the wires were wound around the pad cathode boards
567 using a rotating table and the wires were soldered into place. A wound pad cathode board glued
568 on top to create an sTGC. Holding one sTGC flat with the vacuum, another was glued on
569 top to create a doublet, then two doublets were glued together to create a quadruplet. When
570 gluing sTGCs together, the brass inserts were pushed against alignment pins with the goal of
571 keeping the strip layers aligned within tolerance. However, non-conformities in the shape of
572 the brass inserts, non-conformities in the position of the alignment pins and shifts between
573 sTGCs while the glue cured resulted in misalignments between the brass inserts and strip
574 layers. Precise alignment of the pad boards or wires with respect to the strip boards did
575 not have to be so tightly controlled because pads and wires do not measure the precision
577 coordinate.

578 The Carleton team finished the quadruplets by installing adaptor boards on the angled sides
579 of each layer that allow front end electronics to be attached. Completed quadruplets were
580 sent to McGill University where their performance was characterized with cosmic rays. De-

581 tails pertaining to cosmic ray testing of sTGC quadruplets at McGill University are described
582 in chapter 5. Tested quadruplets were sent to CERN where they were assembled into wedges
583 and alignment platforms installed. The alignment platforms were installed using a jig posi-
584 tioned with respect to the brass inserts. Completed wedges were assembled into sectors then
585 installed on the NSWs.

586 The quadruplet construction process had two steps where strip positions could be shifted off
587 of nominal. At board-level, there could be non-conformities in the etched strip pattern with
588 respect to the brass inserts, described by the four quality parameters [7]. At the quadruplet
589 level, misalignments between the brass inserts and strips on different layers were possibly
590 introduced during the gluing. The result was that the brass inserts were not a reliable
591 reference point and that the strips can be offset from their design position by up to hundreds
592 of micrometers. Offsets in strip positions from nominal in Canadian quadruplets were shown
593 to be random [7], so no one correction would suffice. The offsets must be measured and
594 corrected for in the ATLAS offline software that does the precision tracking. Understanding
595 the work ongoing to make measurements of strip position offsets and correct for them requires
596 understanding the strategy of the NSW alignment system.

597 4.5 NSW alignment

598 The idea of the NSW alignment system is presented in [5], but the details have only been
599 presented internally so far. After the wedges are constructed, alignment platforms are in-
600 stalled on every sTGC quadruplet and optical fibres routed to them, as shown in figure 4.5.
601 Light from the optical fibres will be monitored in real time by cameras (BCAMs) mounted on
602 the alignment bars of the NSWs. The system will thus record the positions of the alignment
603 platforms in the ATLAS coordinate system and any changes over time.

604 The original alignment scheme was to use the brass inserts as a reference between the align-
605 ment platforms and the individual strips, as shown in the solid arrows in figure 4.6 – this
606 will no longer work. The position of the alignment platforms will be known thanks to the
607 alignment system, so a different method to get the position of the strips with respect to the
608 alignment platforms is currently in its final stage of development. The technique consists of
609 the measurement of the strip pattern offset at a few areas on the surface of a sTGC quadru-
610 plet using an xray gun mounted on the alignment platforms. The local strip pattern offset
611 with respect to nominal geometry at the location of each alignment platform is obtained
612 by analyzing the xray gun beam profile. As shown in figure 4.6, this approach essentially
613 bypasses the need to know the position of strips with respect to the brass inserts. The align-
614 ment platforms provide the link to the nominal geometry because the nominal group of strips

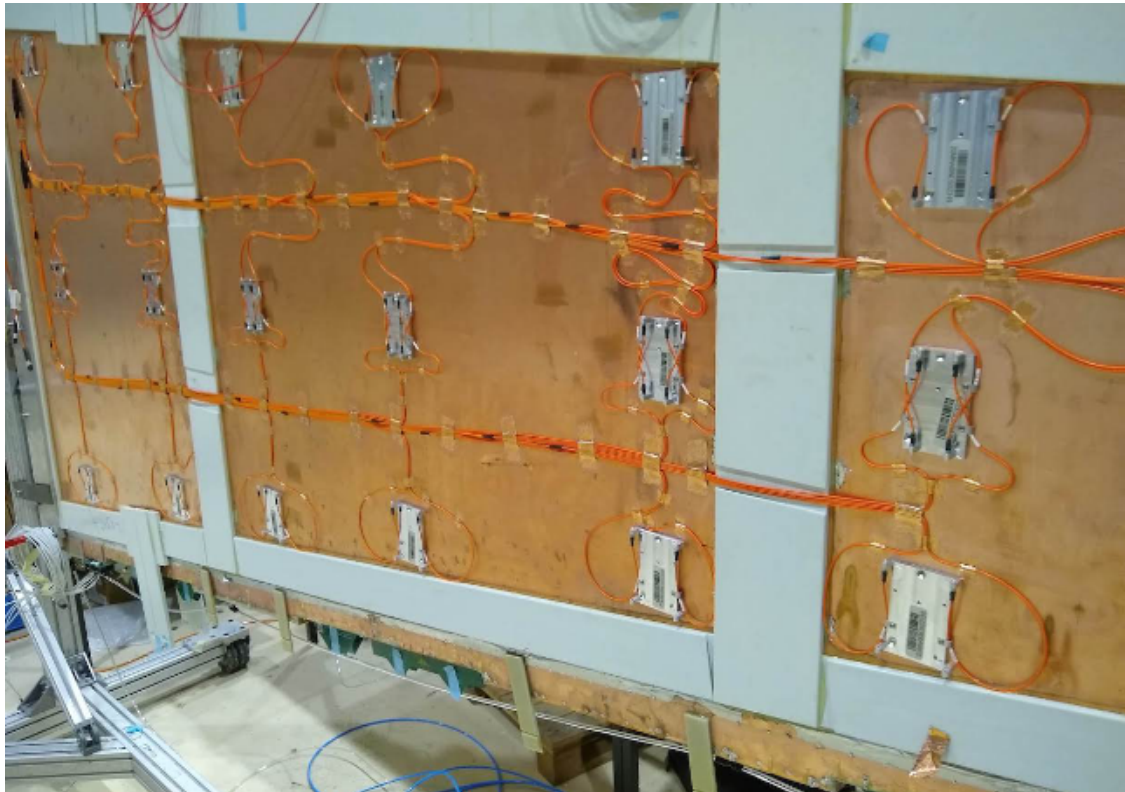


Figure 4.5: A sTGC wedge with alignment platforms (silver) installed on the quadruplet. Optical fibres (orange) are routed to the alignment platforms. Cameras on the frames of the NSWs will record light from the optical fibres to monitor in real-time the position the alignment platforms in the ATLAS coordinate system.

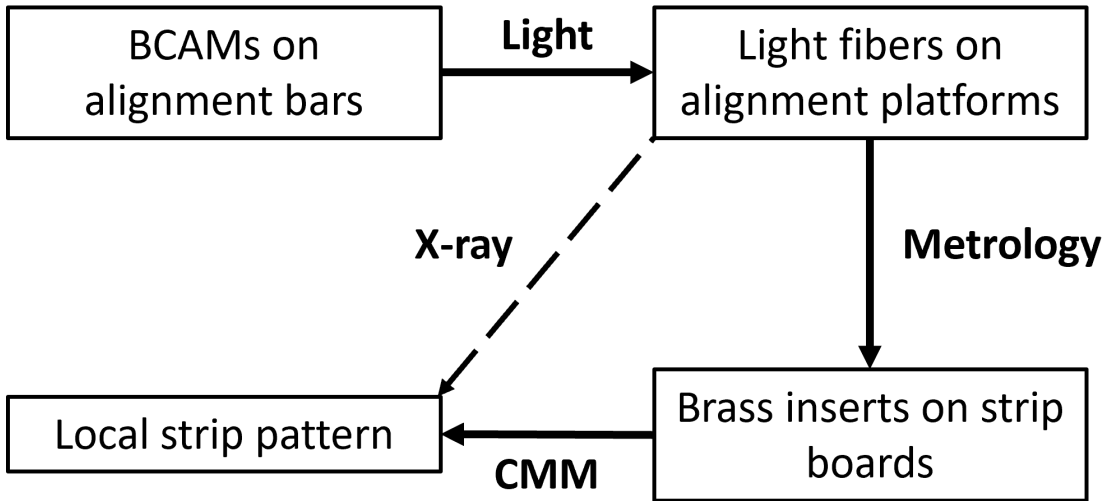


Figure 4.6: Schematic diagram showing how the different elements of the sTGC alignment system relate to one another. The solid arrows denote the planned alignment scheme. The dashed arrow shows the modification being finalized now. This figure was originally designed by Dr. Benoit Lefebvre.

615 that should be nearest to them can be identified using the nominal geometry parameters that
 616 assume the strips are perfectly etched and aligned. Cosmic muon track positions cannot be
 617 compared to the nominal geometry because the alignment platforms are not installed when
 618 cosmics data is collected, so there is no external reference to provide a link to the nominal
 619 geometry.

620 The x-ray method does not have the sensitivity to measure the offset of each strip from
 621 nominal, but what can be measured instead is the offset of the strip pattern in a local area
 622 around the position of the gun. *Local offsets* are used to build an alignment model for each
 623 strip layer. Formally defined, an alignment model is a set of parameters used to estimate the
 624 “as-built” position of a strip given its nominal position. The alignment model currently being
 625 worked on takes x-ray and CMM data as input to calculate an overall offset and rotation of
 626 each strip layer with respect to nominal [8]. The alignment parameters could be described
 627 as “global”, meaning over the whole layer instead of local. Without the x-ray dataset, there
 628 would be no input to the alignment model that takes into account inter-layer misalignments
 629 introduced during quadruplet construction.

630 Given that the x-ray local offsets can only be measured at positions where the gun can
 631 be attached and that they are an important part of the alignment scheme, the new x-ray
 632 measurement technique needs to be validated. The goal of this thesis is to validate the x-ray

⁶³³ local offsets while exploring how cosmics data complements and adds to the understanding
⁶³⁴ of strip positions and global alignment.

⁶³⁵ Chapter 5

⁶³⁶ Using cosmic muons to measure ⁶³⁷ relative strip position offsets

⁶³⁸ At McGill University, among other quality and functionality tests, each Canadian-made
⁶³⁹ quadruplet was characterized with cosmic muons. In this chapter, the experimental setup and
⁶⁴⁰ how the data was analyzed to provide relative strip position offsets is presented. The analysis
⁶⁴¹ method was motivated by the how the measurements could be compared to measurements
⁶⁴² done with the x-ray method (chapter 6) but also stands alone as a characterization of the
⁶⁴³ alignment between strips of different layers. The chapter begins with a brief introduction to
⁶⁴⁴ cosmic rays.

⁶⁴⁵ 5.1 Cosmic rays

⁶⁴⁶ The Earth is being constantly bombarded by particles from the sun, galactic sources and
⁶⁴⁷ extra galactic sources – collectively called cosmic rays [19, 11]. Cosmic rays consist mostly
⁶⁴⁸ of protons, but also heavier ions, gamma rays and the term sometimes includes neutrinos.
⁶⁴⁹ The primary (initial) cosmic ray interacting with the atmosphere causes electromagnetic and
⁶⁵⁰ hadronic showers of secondary particles. Hadronic showers result from the primary cosmic ray
⁶⁵¹ interacting strongly with the target of the atmosphere resulting in an abundant production
⁶⁵² of pions. Charged pions predominantly decay to muons (there is a lesser contribution to
⁶⁵³ the muon flux from kaons as well) [59]. The secondary muons are relativistic and thanks
⁶⁵⁴ to time dilation their lifetime is extended as measured in the reference frame of earth, so a
⁶⁵⁵ flux of approximately 1 muon/cm²/ min reaches the ground [11]. Measuring the muon flux
⁶⁵⁶ and energy spectrum reveals information about primary cosmic rays [59] which is interesting

657 to high energy physicists and astrophysicists. The muon flux is also terribly convenient for
658 testing muon detectors.

659 5.2 Experimental setup

660 Cosmic muon characterization of sTGC quadruplet modules was done with a hodoscope, a
661 complete description of which can be found in [58]. The quadruplet was placed in the center
662 of the test bench. Above and below it was a layer of scintillator-PMT arrays, as shown in
663 figure 5.1. When a cosmic muon passed within the acceptance of the hodoscope, at least one
664 scintillator from the top array and at least one from the bottom array fired in coincidence.
665 A trigger signal was formed using NIM modules from the coincidence of signals from the top
666 and bottom arrays of scintillator detectors. The trigger signal was passed to the front-end
667 electronics attached to the adaptor boards of each layer of the quadruplet.

668 Operating the chambers also required gas and high voltage. A gas mixture of pentane-CO₂
669 in the appropriate proportions was prepared and delivered to each sTGC with a gas system
670 designed and made at McGill University [60]. Since pentane is flammable, the gas system
671 was designed with safety top of mind. The gas system was controlled by a slow control
672 program, also made in-laboratory [60]. To prepare the quadruplets for operation, CO₂ was
673 flushed through them overnight to remove potential impurities within each chamber's gas
674 volume. Then, the equivalent of approximately five sTGC gas volumes of the pentane-CO₂
675 operating gas mixture was flushed through to ensure a uniform gas mixture inside the sTGC;
676 the procedure takes approximately four hours. High voltage was provided by commercial
677 CAEN high voltage boards [60].

678 5.3 Data acquisition

679 Each sTGC electrode was connected to a channel on a prototype ASIC¹ on the front-end
680 electronics, attached to the adaptor boards on each layer of a quadruplet. Each ASIC fea-
681 tures 64 charge amplifiers with selectable gain and input signal polarities, which output the
682 digitized amplitude of the signal at peak for channels above a pre-defined threshold. Thresh-
683 olds were estimated [62] by optimizing the efficiency of detecting muons while minimizing
684 noise, and further manually tuned in the configuration/readout software before the start of
685 data acquisition for each quadruplet module. The signal from the capacitively-coupled strip

¹A custom Application Specific Integrated Circuit (ASIC) named VMM3 [61], designed for the readout of signals from the micromegas and sTGCs of the NSW

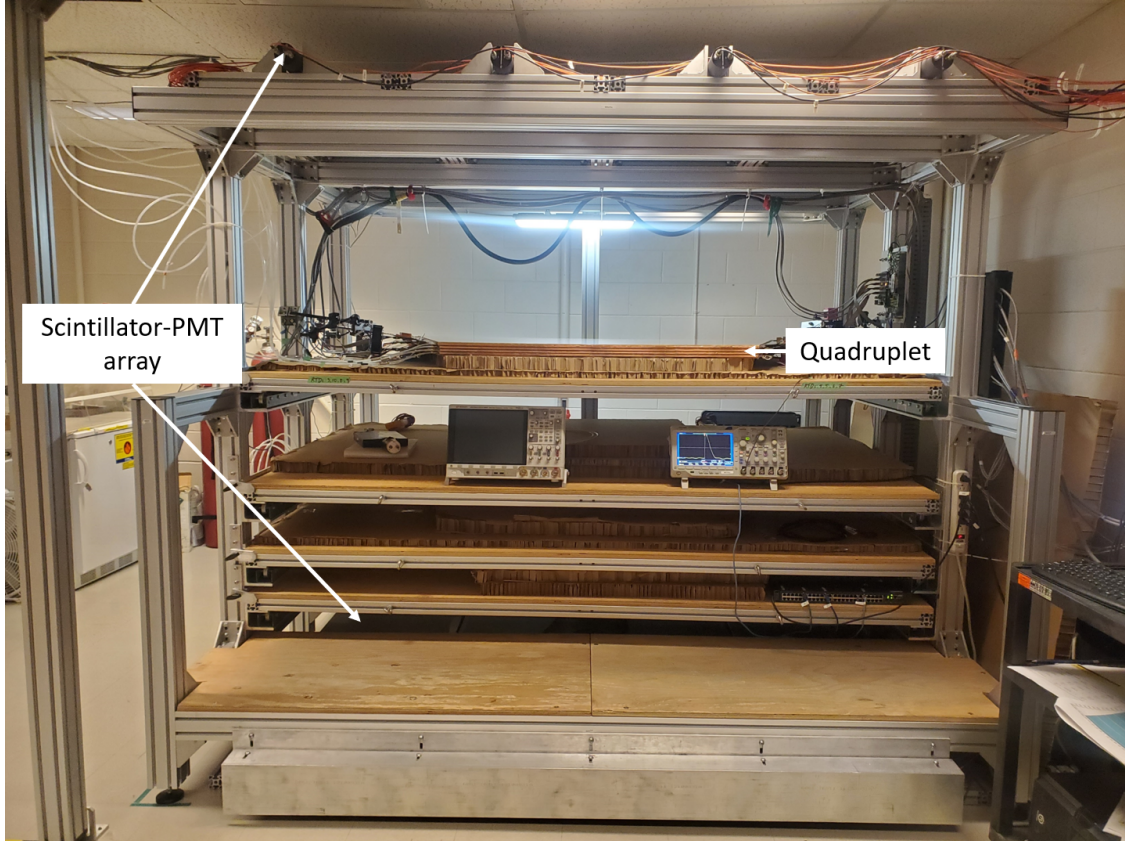


Figure 5.1: Cosmic muon hodoscope at McGill University with a sTGC quadruplet module in the test bench.

686 electrodes has positive polarity and is readout with a gain of one. For each trigger, the
687 signal peak amplitude of all channels above threshold was recorded as an event and stored
688 in a binary file. The readout of strips made use of a special feature of the custom ASIC, the
689 so-called "neighbour triggering" function where signals on channels adjacent to those above
690 threshold are also read out.

691 The quadruplets were held at 3.1 kV for approximately two hours to collect data from
692 approximately 1 million muon triggers.

693 5.4 Data preparation

694 5.4.1 Data quality cuts on electrode hits

695 Corrupted data, if any, is removed while the raw data is being recorded in a binary file.
696 After data taking is completed, the raw data is decoded and electronics channels mapped
697 to physical readout electrodes of the quadruplet. The result of this data preparation step is
698 stored in a ROOT [63] tree data format.

699 A hit is defined as a signal recorded from a channel that was above threshold or (in the
700 case of strips) neighbour triggered. In addition to hits from muons, the quadruplets record
701 noise from the electronics and δ -rays (electrons liberated with sufficient energy to escape a
702 significant distance away from the primary radiation and that produce further ionization).
703 Therefore, selection cuts are applied to reduce the number of hits that do not originate from
704 muons. Readout strips located at the very edge of the cathode board tend to have much
705 higher electronic noise. As a result, all strip hits on a layer where a hit is present on the
706 strips at either edge of the quadruplet are removed from the analysis. A default pedestal
707 value is subtracted from the recorded signal peak amplitude of each electrode for a more
708 realistic estimate of the signal amplitude. Also, events that only have hits on pad electrodes
709 (no strips or wires) were removed from the analysis since these hits are likely from electronic
710 noise, which is higher on the pad readout channels due to their larger area.

711 5.4.2 Clustering and tracking

712 For events passing the quality selection cuts defined in section 5.4.1, the x - and y -coordinates
713 of the ionization avalanche on each layer are extracted from the signal on the wires and strips,
714 respectively, for each event, as shown schematically in figure 5.2. In this work, x is defined
715 as the coordinate perpendicular to the wires and y is defined as the coordinate perpendicular
716 to the strips.

717 The x -coordinate of the muon position is taken as the center of the wire group with the
718 maximum peak signal amplitude, since the wire groups' pitch (36 mm) is larger than the
719 typical extent of the ionization charge generated inside a sTGC. Assuming that the true x -
720 position of the hit is sampled from a uniform distribution over the width of the wire group,
721 the uncertainty in the x -position is approximately $\frac{36}{\sqrt{12}}$ mm = 10 mm [64].

722 The y -coordinate of the muon position is taken as the Gaussian mean of the peak signal am-
723 plitude distribution across groups of contiguous strips. The process of grouping contiguous
724 strip hits on a layer is called clustering, and the resulting group is called a cluster. Figure 5.2
725 sketches the clustering process and a sample cluster is shown in figure 5.3. The data acqui-
726 sition system recorded the identification number of the strip electrode that was hit and in
727 the clustering process the position of the center of the strip electrode is calculated based on
728 the nominal quadruplet geometry. Typically, clusters are built of 3-5 strips. The thickness
729 of the graphite coating over the cathode boards determined how many strips picked up the
730 ionization image charge. Larger clusters can often originate from δ -rays since they spread
731 the ionization charge over a larger area.

732 Events are removed from further analysis if there are two reconstructed clusters on one sTGC,
733 since some hits could be from electronic noise or a simultaneous second muon traversing the
734 chamber. Clusters are rejected if the cluster size is lesser than three strips (which should
735 not happen for real events thanks to neighbour triggering), and if the cluster size is greater
736 than 25. After all quality selection cuts are applied on hits and clusters approximately half
737 of the events recorded remain.

738 The uncertainty on the reconstructed cluster position is assessed by comparing the difference
739 between Gaussian means obtained using two different algorithms. As shown in appendix A.2,
740 the difference between the means from the two algorithms considered is found to be on av-
741 erage approximately 60 μm , larger than the statistical uncertainty on the Gaussian mean
742 obtained from the cluster fit. Therefore, an uncertainty of 60 μm is assigned to the recon-
743 structed y -coordinate of a muon.

744 The reconstructed x and y positions on each quadruplet layer are used to reconstruct a
745 straight track, independently, in the x - z and y - z planes. Tracks are reconstructed using
746 muon coordinates for every possible pair of two sTGC layers. For example, if an event has
747 muon coordinates reconstructed on all four layers, a total of six track segments in the x - z
748 plane and six track segments in the y - z plane will be reconstructed.

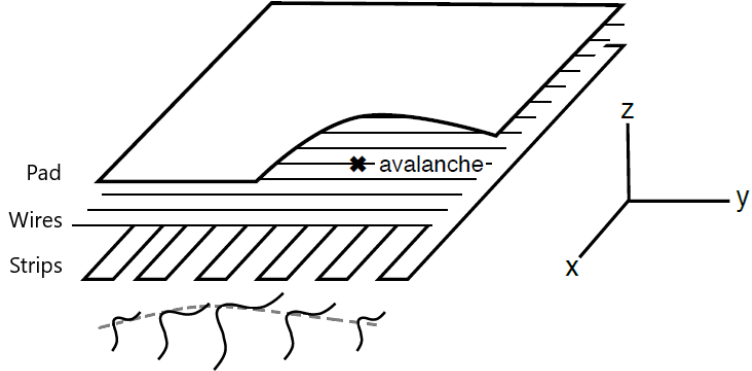


Figure 5.2: Schematic diagram representing the three types of electrodes in a sTGC detector. The position of the ionization avalanche is extracted from the wires and strips that picked up the avalanche signal. The signals on individual strips are sketched. Clustering is the process by which a Gaussian function (represented by the grey dashed line) is fitted to the distribution of the signal amplitude on individual contiguous strips; a sample cluster is shown in figure 5.3. In this work, the $x(y)$ -coordinate will always refer to the coordinate perpendicular to the wires (strips) [58, 56].

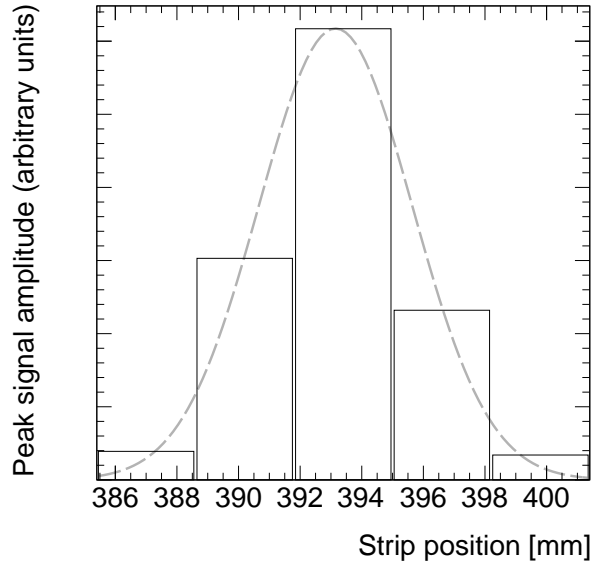


Figure 5.3: A sample cluster resulting from the distribution of ionization signal amplitude recorded on a group of contiguous strips after the passing of a muon. The grey dashed line represents the result of a fit to a Gaussian distribution.

₇₄₉ **5.5 Relative local offsets**

₇₅₀ The offset of a strip from its nominal position can be modeled as a passive transformation.
₇₅₁ The *local offset* is defined as the shift in the strip pattern with respect to nominal geometry
₇₅₂ in a specific area of the sTGC. Local offsets systematically change the set of strips nearest
₇₅₃ to the muons passing through an area. The data preparation software assumes that strips
₇₅₄ are in their nominal positions, so the recorded muon y -coordinate on layer i , y_i , is shifted
₇₅₅ opposite to the layer's local offset, $d_{local,i}$, by

$$y_i = y_{nom,i} - d_{local,i}, \quad (5.1)$$

₇₅₆ where $y_{nom,i}$ is the position of the muon that would have been recorded on layer i if there
₇₅₇ was no local offset. Equation 5.1 ignores other factors that affect the cluster position, like
₇₅₈ position resolution. With cosmics data, there was no external reference to measure $y_{nom,i}$
₇₅₉ and the local offset is unknown. Therefore, only relative local offsets can be measured.

₇₆₀ To measure relative local offsets, two of the four sTGC layers are chosen to provide the
₇₆₁ reference coordinate system with respect to which local offsets are calculated. The hits on
₇₆₂ the chosen two reference or fixed layers were used to create tracks that can be interpolated
₇₆₃ or extrapolated (polated) to the other two layers. The set of two fixed layers and the layer
₇₆₄ polated to are referred to as a tracking combination. The residual of track i , Δ_i , is defined
₇₆₅ as,

$$\Delta_i = y_i - y_{track,i}, \quad (5.2)$$

₇₆₆ where $y_{track,i}$ is the polated track position on the sTGC layer at which the residual is mea-
₇₆₇ sured. Track residuals are affected by the relative local offset in the area of each layer's hit.
₇₆₈ As an example, in figure 5.4, the residual on layer 2 perhaps indicates that layer 2 is offset
₇₆₉ with respect to layers 1 and 4 in the area of the track. Of course, a single track residual
₇₇₀ says nothing of the real relative local offset because of the limited spatial resolution of the
₇₇₁ detectors and fake tracks caused by noise or delta rays. However, the mean of residuals for
₇₇₂ all tracks in a region of interest will be shifted systematically by the local offsets between
₇₇₃ layers [58]. For a quadruplet with nominal geometry, the mean of residuals should be zero in
₇₇₄ all regions and for all reference frames, unlike the example regions in figure 5.5. The value
₇₇₅ of the mean of residuals is a measure of the relative local offset of the layer with respect to
₇₇₆ the two fixed layers used to reconstruct the muon track. The sign convention is such that
₇₇₇ the mean of residuals is opposite to the relative local offset.

₇₇₈ To study the relative local offsets, residual distributions across each strip layer of a quadruplet
₇₇₉ for all possible tracking combinations are assembled and fitted. As expected, the residual dis-
₇₈₀ tributions are wider for tracking combinations where the extrapolation lever arm is largest,

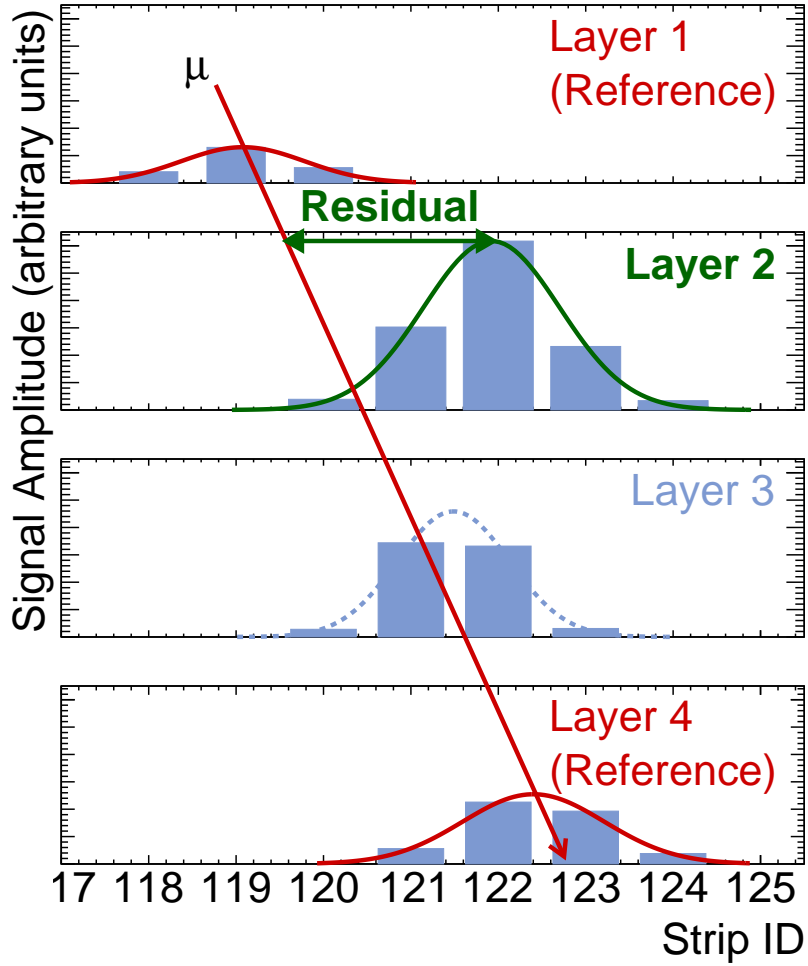
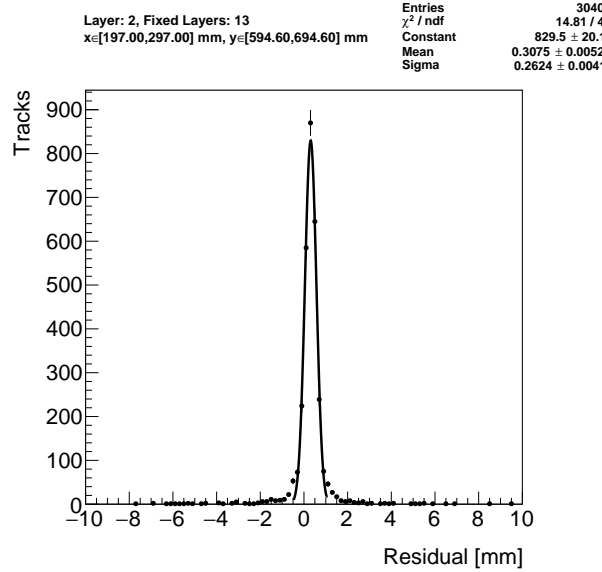
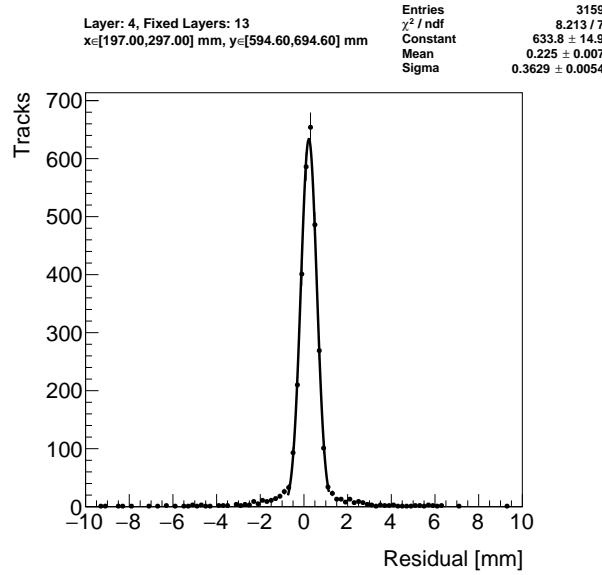


Figure 5.4: Representation of a muon event recorded by an sTGC quadruplet. The charge clusters measured using strip electrodes are fit with a Gaussian distribution and the fitted mean is taken as the reconstructed muon position. A track is built from the chosen reference layers, 1 and 4, and the track residual is calculated on layer 2. The clusters come from a real muon, but their positions were modified to highlight the non-zero value of the residual on layer 2.



(a) Tracks on layer 2, reference layers 1 and 3.



(b) Tracks on layer 4, reference layers 1 and 3.

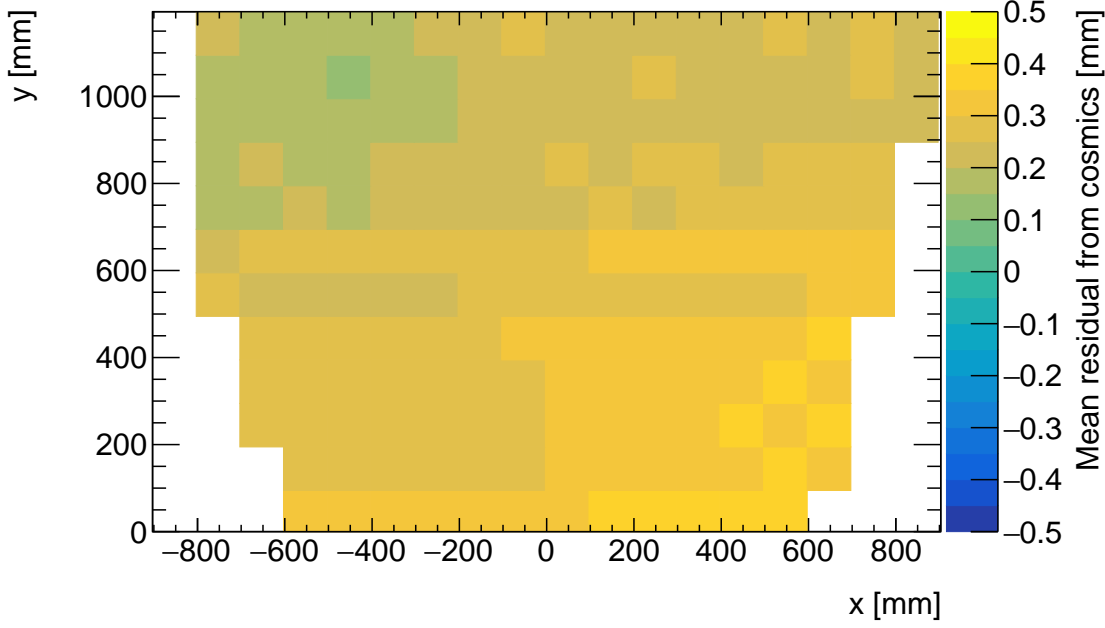
Figure 5.5: Residual distribution in the region $x \in [197, 297]$ mm, $y \in [594.6, 694.6]$ mm (100 mm by 100 mm area) for two different tracking combinations. Data from quadruplet QL2.P.11.

781 as in the example distributions shown in figure 5.5. In general, residual means from dis-
782 tributions of residuals with geometrically less favourable tracking combinations have larger
783 statistical and systematic uncertainties. The bin size of 200 μm for the distributions shown
784 in figure 5.5 was chosen based on the uncertainty on residuals calculated from tracks on layer
785 4 (1) built from hits on layers 1 and 2 (3 and 4) given a cluster y -coordinate uncertainty of
786 60 μm (discussed in section 5.4.2 and appendix A.3), since these tracks yield residuals with
787 the largest uncertainties.

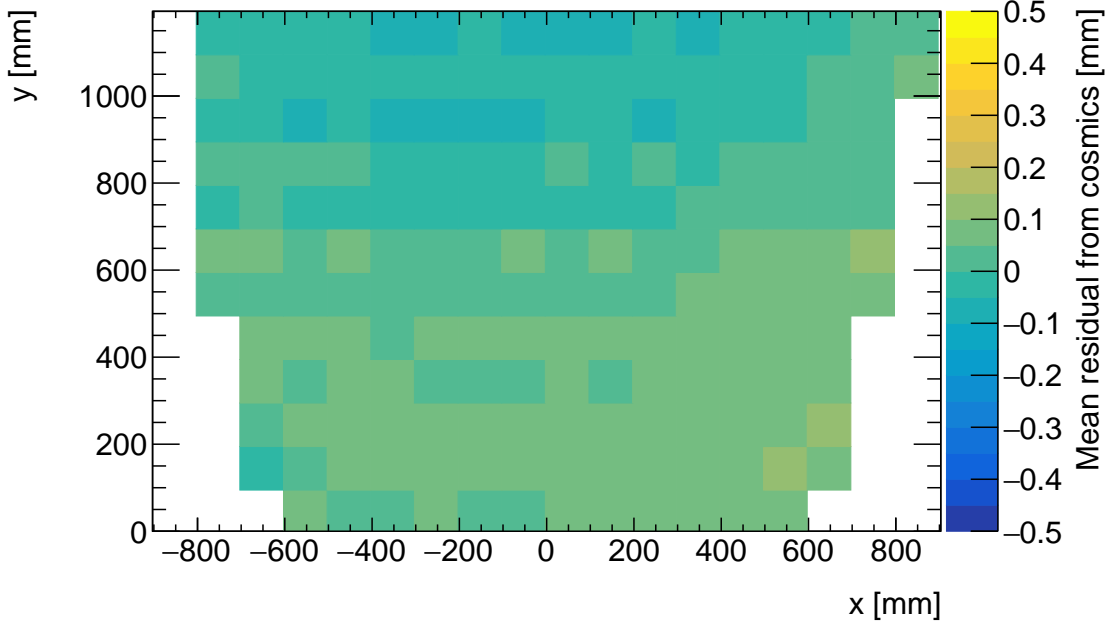
788 A fit to a Gaussian distribution is used to extract the mean of the residual distributions.
789 The residual distributions are actually better modeled by a double Gaussian distribution
790 that better captures the distribution tails in figure 5.5. However, a study described in
791 appendix C.1 found that a fit to a single Gaussian function in the core of the distribution is
792 sufficient to reconstruct the mean of the distribution.

793 The area of the region of interest where tracks residuals were included in the residual distri-
794 bution was 100 mm by 100 mm. The size balanced the number of tracks falling in the region
795 of interest to give a small statistical uncertainty on the fitted mean while being smaller
796 than the order on which local offsets were expected to change significantly. “Significantly”
797 was defined as 100 μm , the required position resolution of the sTGCs and the precision to
798 which strip positions should be known. The distance over which local offsets are expected to
799 change significantly can be estimated using a simple alignment model. Assuming the strips
800 of a layer have been displaced uniformly from their nominal positions by a global offset and
801 rotation, the distance in x a large but possible rotation of 1 mrad changes the local offset by
802 100 μm is 100 mm.

803 The mean of residuals is plotted across each strip layer for every possible tracking combina-
804 tion to get a picture of the how relative local offsets change as a function of position over
805 the layer’s surface. Figure 5.6 shows the mean of residuals on layer 2 calculated with layers
806 1 and 3 as reference for two different quadruplets, referred to as QL2.P.11 and QL2.P.8. In
807 figure 5.6a, the Gaussian mean of the residual distribution in figure 5.5a is the entry in the
808 bin defined by boundaries $x \in [197, 297]$ mm, $y \in [594.6, 694.6]$ mm.



(a) Mean of track residuals on layer 2, obtained using layers 1 and 3 as reference, for QL2.P.11.



(b) Mean of track residuals on layer 2, obtained using layers 1 and 3 as reference, for QL2.P.8.

Figure 5.6: Mean of residuals in each 100 mm by 100 mm bin over the area of sTGC layer 2. The entry in $x \in [197, 297]$ mm, $y \in [594.6, 694.6]$ mm of figure 5.6a corresponds to the fitted Gaussian mean in figures 5.5a. The mean of residuals has the same value and opposite sign to the relative local offset of layer 2 with respect to the reference frame defined by layers 1 and 3.

Many of the residual means are non-zero and change smoothly over layer 2, indicating that there are relative local offsets stemming from global misalignments between the strip patterns of different sTGC layers in both quadruplets. Given that the residual mean changes with x in figure 5.6a, quadruplet QL2.P.11 likely has a rotation of layer 2 with respect to layers 1 and 3, combined with an offset of the entire layer. The residual means are smaller in figure 5.6b indicating that quadruplet QL2.P.8 is less misaligned overall than QL2.P.11; however the relative local offsets range between $\pm 200 \mu\text{m}$ so they are significant enough to warrant correction strip positions to achieve the required track angular resolution in the NSW.

5.6 Systematic uncertainty

The statistical uncertainty on the local residual means was typically around 10 - 20 μm , and appendix B shows that the analysis is not statistically limited by the number of triggers collected for each quadruplet. Systematic uncertainties were found to be larger than the statistical uncertainty on the residual means.

The differences in fitted local residual means when calculated in different ways were studied in detail in appendix C. Systematic uncertainties are assigned per tracking combination as the root-mean-square (RMS) of the distribution of the difference in residual means. For example, the RMS associated with fitting the local residual distributions with a Gaussian or double Gaussian is 25 μm for the geometrically least favourable tracking combinations. The distribution is shown in appendix C.1. For geometrically similar tracking combinations (like: tracks on layer 1 built from hits on layers 3 and 4, and tracks on layer 4 built from hits on layers 1 and 2), the systematic uncertainty was assigned as the average RMS of both.

Other choices were: whether to use data collected at 2.9 kV or 3.1 kV (both are collected at McGill); what cluster fitting algorithm to use; and whether or not to apply a differential non-linearity (DNL) correction to the cluster y -positions [6]. A systematic uncertainty was assigned using the method above to account for the effect of each choice and quantify the robustness of the mean of residuals. The reasons for each choice are listed below.

Data taken at 3.1 kV was used over 2.9 kV because the strip and wire tracking efficiency increases with higher voltage [58] (appendix C.2).

The Minuit2 package [65] was used to fit clusters over Guo's method [66] because it provided automatic statistical uncertainty estimates and is the standard fit algorithm of ROOT [63] (appendix C.3).

The DNL correction was not applied because its effect on the residual means was negligible (appendix C.4).

Tracking geometry	Residual distribution fit function (C.1)	Cosmics data collection voltage (C.2)	Cluster fit algorithm (C.3)	Apply DNL correction or not (C.4)	Total
Similar to layer 3, fixed layers 1, 2	0.01	0.04	0.02	0.01	0.05
Similar to layer 4, fixed layers 1, 2	0.03	0.01	0.03	0.01	0.10
Similar to layer 2, fixed layers 1, 3	0.01	0.02	0.01	0.000	0.03
Similar to layer 4, fixed layers 1, 3	0.01	0.04	0.01	0.01	0.04
Similar to layer 2, fixed layers 1, 4	0.01	0.04	0.01	0.01	0.04

Table 5.1: Systematic uncertainty assigned for each analysis option, detailed in appendix C.

843 A summary of the systematic uncertainties assigned to the mean of residuals for each tracking
 844 combination is given in table 5.1.

845 The uncertainty in each mean of residuals was assigned as the sum in quadrature of the sta-
 846 tistical uncertainty in the mean and the appropriate systematic uncertainty for the tracking
 847 combination.

848 5.7 Discussion

849 Cosmics data is being used to calculate relative alignment parameters using two other meth-
 850 ods [58]. The results of this analysis could be cross-checked with the other methods; however
 851 the studies in appendix C show that the residual means are robust, so the comparison was
 852 not prioritized.

853 Given that the uncertainty in the residual means is lesser than or near to the order of the

854 required position resolution of the sTGCs ($100\text{ }\mu\text{m}$ [5]) they are relevant input for alignment
855 studies.

856 The relative local offsets as calculated from the mean of residual distributions provide a
857 complete picture of the relative alignment between detectors planes. In fact, cosmic muon
858 testing is the only characterization technique where the entire surface of quadruplet layers
859 can be probed since muons hits are distributed almost uniformly; the CMM [7] and x-ray
860 methods [8] depend on measurements at reference points, and test beams only have a limited
861 beam spot [6]. By looking at 2D-histograms of residual means like figure 5.6 for all tracking
862 combinations, it is easy to identify quadruplets that suffer large relative misalignment since
863 many residual means differ significantly from zero. Moreover, the pattern in the residual
864 means can be used to motivate a physical interpretation of misalignments. The residual
865 means can be used as a reference, cross check, or input in other alignment studies.

866 Relative local offsets cannot be used to position strips in the absolute ATLAS coordinate
867 system because there was no external reference to measure positions on all layers with re-
868 spect to. The lack of external reference means that there is not enough information to unfold
869 relative local offsets into absolute local offsets (with respect to the nominal quadruplet ge-
870 ometry). As an example, assuming that the residual on layer 2 in figure 5.4 is representative
871 of the absolute value of the relative local offset, the residual on layer 2 could be caused by
872 the strips on layer 2 being misaligned from nominal, but it could also be caused by strips
873 on layers 1 and 4 being offset from nominal while the strips on layer 2 are in their nominal
874 positions! Any number of combinations of local offsets on layers 1, 2 and 4 could produce
875 the residual on layer 2. Absolute local offsets must be calculated another way.

876 **Chapter 6**

877 **Using x-rays to measure relative strip
878 position offsets**

879 Local offset measurements were done with the x-ray method. The reader is referred to the
880 paper describing the x-ray method [8], although some minor changes have been made to the
881 experimental setup since it was written. The experimental setup described here is current
882 and was used to collect the data presented in this thesis.

883 **6.1 Experimental setup**

884 The x-ray tests were performed after the quadruplets arrived at CERN, were assembled into
885 wedges, and alignment platforms installed. Essentially, an x-ray gun was attached to one
886 of the alignment platforms glued to the surface of the wedge and the x-ray beam profile
887 recorded by the strips.

888 The wedges were installed on carts that could rotate their surface to a horizontal position. A
889 mounting platform was installed on top of the alignment platform using a three-ball mount.
890 The x-ray gun used was an [Amptek Mini-X tube](#). The gun was placed in a brass holder
891 with built-in 2 mm collimator and 280 μm copper filter. The holder was mounted on one
892 of five positions on the mounting platform, as shown in figure 6.1. Gun positions were
893 chosen to avoid wire support structures in the sTGCs that reduce hit efficiency [58] and
894 boundaries between sets of strips read out by two different ASICs that could each have
895 different thresholds.

896 As with cosmics data collection, each sTGC also needed gas and high voltage to operate.

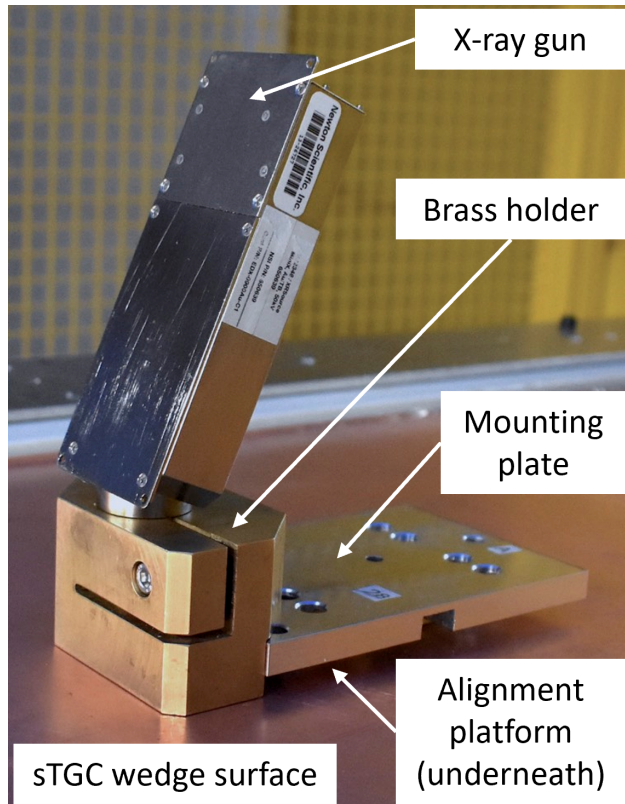


Figure 6.1: The x-ray gun mounted to the alignment platform on the surface of the wedge.
Adapted from [8].

897 Each layer was operated at 2.925 kV with high voltage from a NIM crate. The chambers
898 were flushed with CO₂ before and during data collection.

899 The gun produced x-rays with energies under 40 keV with peaks in the 7-15 keV range. Peaks
900 in the 0-30 keV range were filtered out by the copper filter and the copper of the sTGCs.
901 The x-rays mostly interacted with the wedge's copper electrodes and gold-plated tungsten
902 wires via the photo effect. The resulting photoelectrons caused ionization avalanches that
903 were picked up by the strips.

904 6.2 Data acquisition

905 A different version of the same front end electronics, but the same ASIC, as used in cosmics
906 testing were used for the x-ray testing to amplify the electrode signals and measure the peak
907 signal amplitude. Data was collected for two minutes per gun position with random triggers.
908 A trigger recorded all signals above threshold. Pad and wire data was not recorded.

909 6.3 Data preparation

910 Like with cosmics analysis, a default pedestal is subtracted from the signal peak amplitude
911 on each electrode.

912 Clusters are defined as groups of contiguous strip hits collected within 75 ns. The peak signal
913 amplitude of each electrode in a cluster is fit with a Gaussian, and the mean of the Gaussian
914 is taken as the cluster position. Cluster positions are corrected for DNL (see definition in
915 appendix C.4). Only clusters composed of hits on 3-5 strips were used in the x-ray analysis.
916 Clusters with signal on more than 5 strips were cut because they were most likely caused by
917 photoelectrons ejected with enough energy to cause more primary ionization and subsequent
918 avalanches as δ -rays.

919 The x-ray analysis diverges entirely from the cosmics analysis algorithm here because the x-
920 rays do not leave tracks. The signals picked up by the strips are from ionization avalanches [54]
921 generated by photoelectrons liberated from the metals of the sTGCs, which only travel
922 through one gas volume and are ejected at all angles. Instead of creating tracks, the cluster
923 position distribution on each layer is used to define the beam profile. A typical beam profile
924 is shown in figure 6.2.

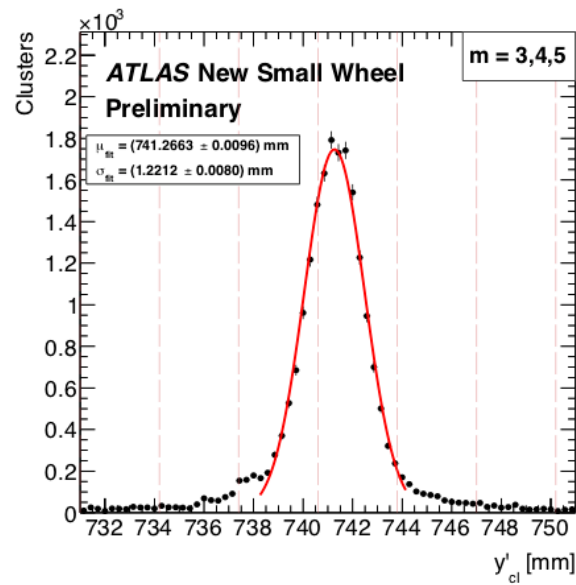


Figure 6.2: Distribution of x-ray cluster mean positions after the analysis cuts and corrections. The strip cluster multiplicity, m , was limited to 3, 4 and 5. The red curve is a Gaussian fit of the distribution and the pink dashed lines denote the edges of the strips [8].

925 6.4 Measuring local offsets

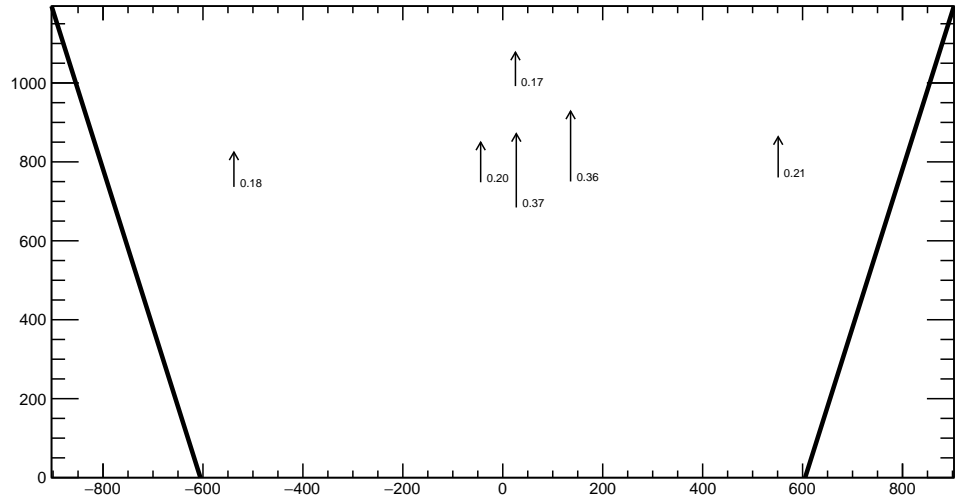
- 926 The mean of the cluster position distribution is taken as the x-ray beam profile center. The
927 expected center is calculated for each gun position using the nominal quadruplet geometry
928 parameters. The nominal position is corrected for the geometry of the brass holder and the
929 positioning and angle of the alignment platforms and the beam angle. The difference between
930 the expected and reconstructed beam profile center is a measure of the local offset. Applying
931 the logic of equation 5.1 to the beam profile, the Gaussian mean of cluster positions on the
932 given layer acts as the recorded position, y_i , the expected center is $y_{nom,i}$ and the local offset
933 is $d_{local,i}$ as before, where i denotes the layer. Since the position of the alignment platforms
934 will be monitored by the alignment system in ATLAS [5], the position of the strips that
935 should have been at the gun position are shifted by $d_{local,i}$ and so are known in the ATLAS
936 coordinate system for every position where x-ray data was taken.
- 937 The x-ray working group accepted an uncertainty of 120 μm on the beam profile centers. The
938 largest uncertainty comes from the effect of the gun angle, which proved difficult to measure
939 and correct for.
- 940 The local offsets are not presented here as the author did not conduct this work. However,
941 the author used the local offsets to calculate relative local offsets.

942 6.5 Measuring relative local offsets

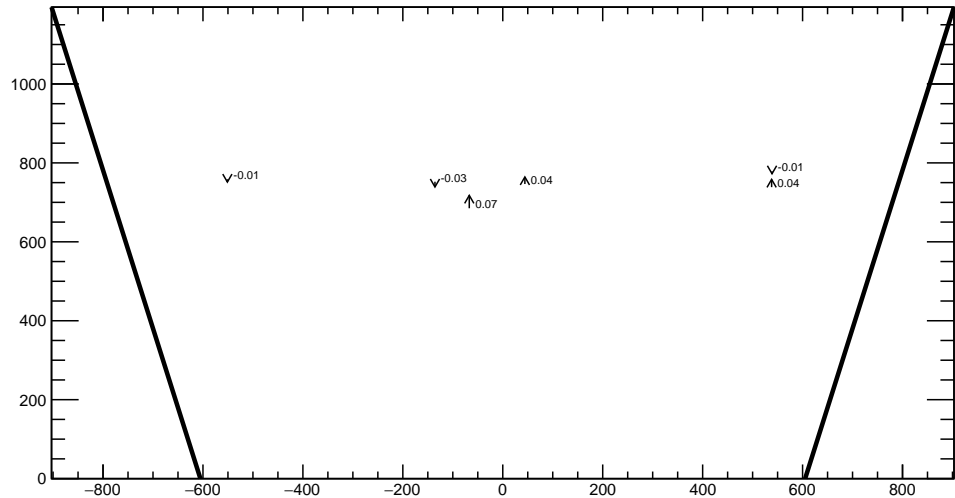
- 943 The x-ray local offsets were shown to be correlated with the local offsets calculated from
944 the CMM data, but the CMM data does not include the effect of inter-layer misalignments
945 so the degree of correlation measurable was limited. Cosmics data is affected by inter-layer
946 misalignments. Since the local offsets for x-rays and cosmics data are measured in different
947 coordinate systems, they cannot be compared directly. Bringing the cosmics relative local
948 offsets into an absolute coordinate system is impossible; however, the x-ray local offsets can
949 be brought into a relative coordinate system.
- 950 The measured x-ray beam profile centers were systematically affected by local offsets in the
951 same way as the mean cosmics residuals, as modeled by equation 5.1. Therefore, if a 2-layer
952 track is built from the beam profile centers on each layer and the residual calculated on a
953 third layer, that residual should match the local mean cosmics residual. The residual is the
954 difference between the beam profile center on the layer of interest and the polated track
955 position from the beam profile centers recorded on the two fixed layers. The beam profile
956 center on the layer of interest acts as y_i and the polated track position acts as $y_{track,i}$ in
957 equation 5.2.

958 The track referred to here is not an actual track of the x-ray beam. A beam profile center
959 is actually the Gaussian mean of all selected mean cluster positions recorded during the
960 x-ray data taking period, not a single hit of a track. Building an “abstract” track was
961 necessary because the x-rays cause signal in the chamber via the photoeffect so there were
962 not individual “x-ray tracks” to record. In fact the x-ray data could be collected separately
963 for each layer. Nonetheless, since the effect of local offsets on the beam profile centers was
964 the same as their effect on the cosmics cluster positions the difference in algorithm between
965 x-ray and cosmics analysis was allowed.

966 For each x-ray survey position, the x-ray residual was calculated for all possible tracking
967 combinations (which required an x-ray beam profile on at least three layers). The x-ray
968 residuals on layer 2 calculated from the beam profile centers recorded on layers 1 and 3 are
969 represented as arrows for QL2.P.11 and QL2.P.8 in figure 6.3. For QL2.P.11, a negative
970 relative local offset at all x-ray survey positions is clear.



(a) QL2.P.11 x-ray residuals on layer 2, reference layers 1 and 3.



(b) QL2.P.8 x-ray residuals on layer 2, reference layers 1 and 3.

Figure 6.3: The x-ray residuals on layer 2 calculated from the beam profile centers recorded on layers 1 and 3 for QL2.P.11 and QL2.P.8. The arrows originate from the expected position of the beam profile center assuming a nominal geometry, and the lengths are proportional to the calculated x-ray residuals. The value of the x-ray residuals are annotated in millimeters and have an uncertainty of ± 0.15 mm.

971 The uncertainty on the x-ray residuals was the error propagated through the tracking, taking
972 an uncertainty of 120 μm on each beam profile center. The uncertainty on the x-ray residuals
973 ranged from 0.15 mm to 0.4 mm from the most to least geometrically-favourable tracking
974 combination. There is no discernible pattern to the x-ray residuals on QL2.P.8 because they
975 have absolute values smaller than the uncertainty on the x-ray residuals. The x-ray residual
976 uncertainties are significantly larger than the uncertainties on the mean cosmics residuals.

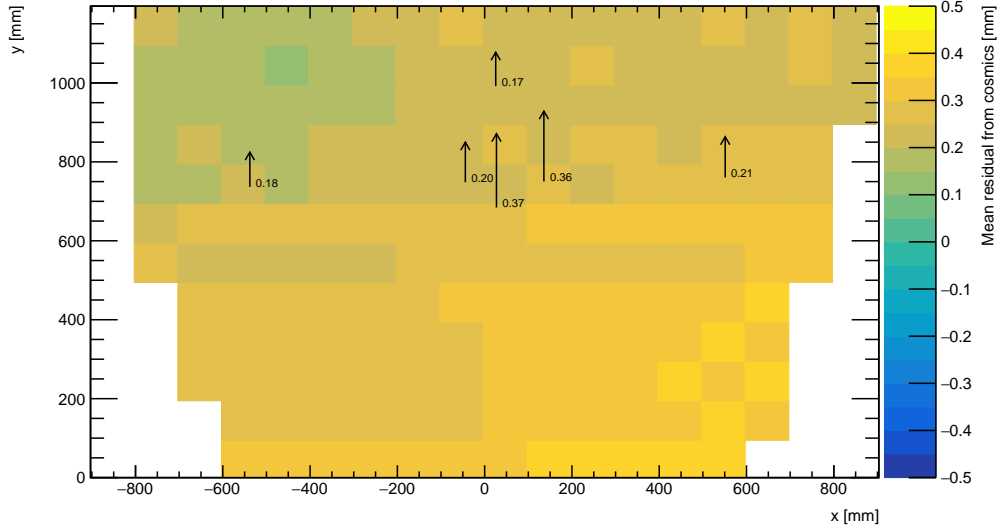
977 **Chapter 7**

978 **Comparing cosmic muon and x-ray
979 relative strip position offsets**

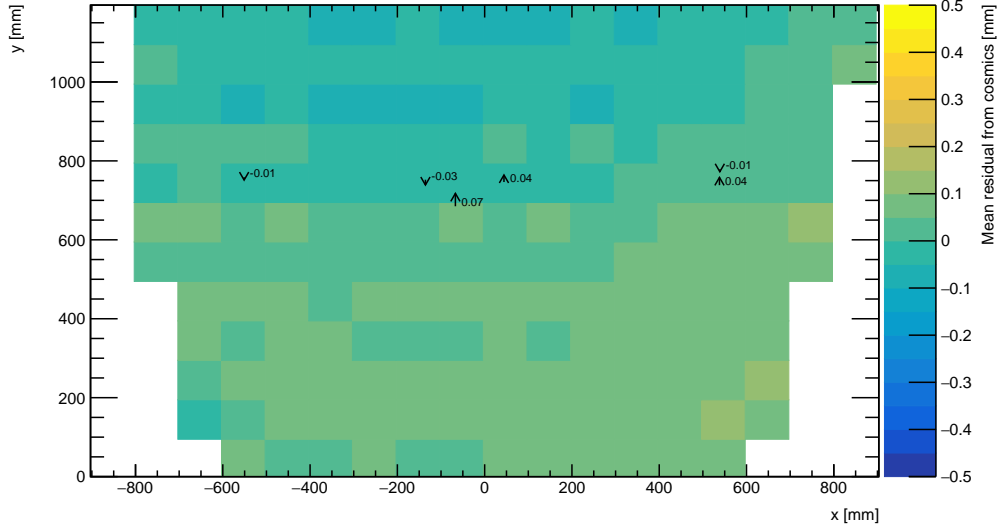
980 The goal was to validate the local offsets extracted from the x-ray data with cosmics data.
981 The complication was that the x-ray dataset provided absolute local offsets while the cosmics
982 dataset provided relative local offsets, which could not be compared directly. The solution
983 was to use the x-ray local offsets to calculate relative local offsets. The x-ray relative local
984 offset is opposite sign to the x-ray residual reconstructed from an abstract track using the
985 beam profile centers on each layer as the track hits. The cosmics relative local offset was
986 inferred from the Gaussian mean of muon track residuals in a 100 mm by 100 mm area,
987 referred to the as the mean cosmics residual. Residuals of each type calculated using the
988 same reference layers are compared for each area where x-ray data is available. The results
989 of the comparison are presented here.

990 **7.1 Assessing correlation**

991 The 2D visualizations of the mean cosmics and x-ray residuals for tracks on layer 2 with
992 reference layers 1 and 3 on QL2.P.11 and QL2.P.8 are shown in figure 7.1. Figure 7.1 is a
993 superposition of figures 5.6 and 6.3.



(a) QL2.P.11 residuals of tracks on layer 2, reference layers 1 and 3.



(b) QL2.P.8 residuals of tracks on layer 2, reference layers 1 and 3.

Figure 7.1: The mean cosmics residuals are shown using colour. The x-ray residuals available at nominal gun positions are drawn as arrows and the value of the residual annotated in millimeters with uncertainty ± 0.15 mm. The length of the arrows is 500 times the value of the x-ray residual, scaled for visibility. These plots are a superposition of figures 5.6 and 6.3.

994 Figure 7.1a shows that for QL2.P.11 the x-ray residuals are of the same sign and order as the
995 mean cosmics residuals, as can be seen by comparing the the annotated value of the x-ray
996 residual to the mean cosmics residual represented by colour; QL2.P.11's mean cosmics and x-
997 ray residuals are correlated to some degree. For QL2.P.8, the x-ray residuals are of the right
998 order compared to the mean cosmics residuals, but the correlation is not apparent. While
999 x-ray residuals do not reveal a pattern in relative local offset across the layer's surface, the
1000 mean cosmics residuals show a structure to the relative local offsets since they vary smoothly
1001 over the surface of layer 2.

1002 The comparison of mean cosmics and x-ray residuals was done for several quadruplets for all
1003 tracking combinations (not just layer 2 residuals calculated with fixed layers 1 and 3 like in
1004 figure 7.1). Scatter plots of the x-ray and mean cosmics residuals on QL2.P.11 and QL2.P.8
1005 for all tracking combinations shown in figures 7.2 and 7.3 reveal the degree of correlation
1006 between the datasets. In the correlation plots, each rectangle is centered on the value of a
1007 mean cosmics and x-ray residual pair calculated with a given tracking combination for every
1008 gun position where data is available; the height and width of the squares are the uncertainty
1009 in the mean cosmics and x-ray residuals respectively. Note that in the scatter plots, the
1010 regions of interest where cosmics tracks are included in the calculation of mean of residuals
1011 are exactly centered on the nominal x-ray beam position, unlike in figure 7.1.

1012 The fitted slope and offset in figure 7.2 show that the two QL2.P.11 datasets are correlated.
1013 The large uncertainty on the x-ray residuals set a limit on the sensitivity of the analysis,
1014 for if the absolute value of the x-ray residuals of a quadruplet were smaller than the x-ray
1015 residual uncertainties, no conclusion about the correlation could be drawn, like for QL2.P.8
1016 (figure 7.3). This result is reflected in the small x-ray residuals shown in figure 7.1b that
1017 do not reveal a pattern in the relative local offsets across the surface of layer 2. However,
1018 figure 7.3 shows that the x-ray and mean cosmics residuals are clustered around zero, as is
1019 expected for a quadruplet with small relative misalignments between layers.

1020 There are three patterns in the residuals on the scatter plot explained by geometry. First,
1021 for both datasets the uncertainty in the extrapolated track residuals were larger than the
1022 interpolated track residuals because of the extrapolation lever arm. For the x-ray residuals,
1023 the effect of the lever arm on the uncertainty was direct since the residual was calculated from
1024 a single abstract track; for the mean cosmics residuals it was the widening of the residual
1025 distribution due to the extrapolation lever arm that increased the uncertainty in the fitted
1026 mean of residuals. Second, residuals calculated through extrapolation tend to be larger
1027 because the extrapolation lever arm can produce more extreme values of the track position
1028 on the layer of interest. Third, the points in figure 7.2 are geometrically correlated (e.g.
1029 they seem to be roughly mirrored around the origin). This is expected since the residuals
1030 calculated using a given set of three layers should be geometrically correlated by the local

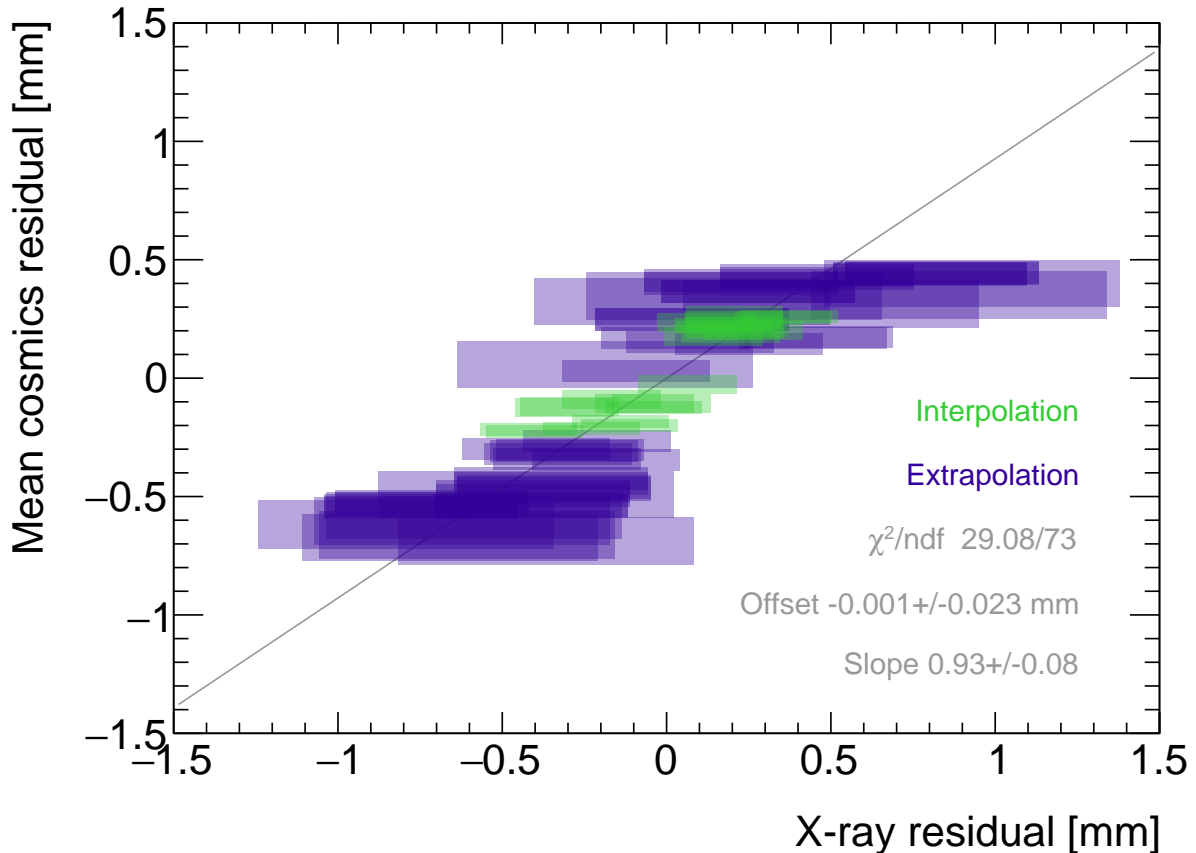


Figure 7.2: Correlation plot between x-ray and mean cosmics residuals for all tracking combinations for QL2.P.11. Each rectangle is centered on an x-ray and mean cosmics residual pair calculated at a given gun position and for a certain tracking combination. The width of the rectangles in x and y are the uncertainty in the x-ray and mean cosmics residual respectively. A printer-friendly version of this plot is available in appendix D.

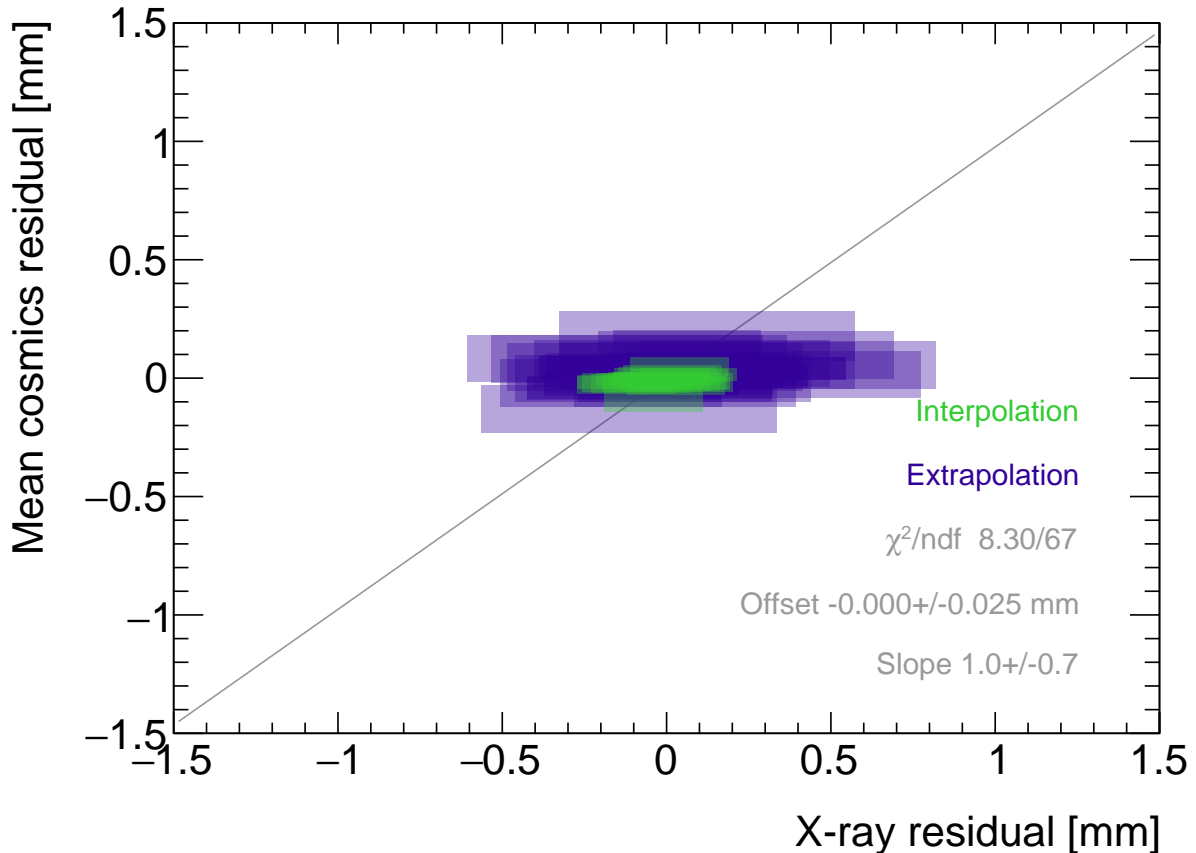


Figure 7.3: Correlation plot between x-ray and mean cosmics residuals for all tracking combinations for quadruplet 2. Each rectangle is centered on an x-ray and mean cosmics residual pair calculated at a given gun position and for a certain tracking combination. The width of the rectangles in x and y are the uncertainty in the x-ray and mean cosmics residual respectively. A printer-friendly version of this plot is available in appendix D.

1031 offsets on each layer (the $d_{local,i}$ on each layer as defined in equation 5.1).

1032 7.2 Discussion

1033 Several quadruplets were tested for each quadruplet construction geometry built in Canada.
1034 Each quadruplet fell into one of the two categories: residuals large enough to see a correlation,
1035 or residuals too small to see a correlation. Since the x-ray and mean cosmics residuals can
1036 be used to calculate relative local offsets between the layer and the two reference layers,
1037 quadruplets with the largest relative misalignments had the largest range of residuals. The
1038 correlation plots are another easy visual way to identify quadruplets with large relative
1039 misalignments.

1040 The most significant limit on measuring the degree of correlation between the x-ray and
1041 mean cosmics residuals was the uncertainty on the x-ray residuals, which stemmed from the
1042 systematic uncertainty of 120 μm in the x-ray beam profile centers used to build the abstract
1043 tracks. For example, in figure 7.3, if the x-ray residuals could be known to within better
1044 precision, perhaps they would be correlated with the mean cosmics residuals. The x-ray
1045 method was limited primarily by the systematic uncertainties in the relative alignment of
1046 the platforms and the gun, especially the gun angle.

1047 The analysis of certain quadruplets was limited by the availability of data. Sometimes,
1048 less than three layers were surveyed for a given x-ray gun position so no residuals could
1049 be calculated. Too few x-ray residuals prevented the analysis from detecting a significant
1050 correlation, should it even be measurable. Often, the analysis of smaller quadruplets (placed
1051 innermost on the wheel) suffered as a result because they had fewer alignment platforms, and
1052 hence gun positions, on their surfaces. The analysis was also limited to certain quadruplets.
1053 The wedges constructed the earliest (typically small wedges) were surveyed when the x-ray
1054 method was still being designed and so have limited x-ray residuals calculated from beam
1055 profiles of lower quality. In addition, not all cosmic muon test sites had enough front end
1056 electronics to collect data on three layers simultaneously, which is the minimum required to
1057 be able to calculate residuals.

1058 Nonetheless, the comparison of x-ray and cosmics residuals was really to confirm the x-ray
1059 method's ability to measure local offsets with an independent dataset. The x-ray local offsets
1060 allow the calculation of relative local offsets that have been correlated to the cosmics relative
1061 local offsets. Therefore, the analysis of quadruplets with relative local offsets large enough
1062 to detect a correlation validates the x-ray method's ability to measure local offsets.

1063 The potential of using relative local offsets calculated from cosmics data to study relative
1064 alignment between sTGC layers stands on its own. For example, although the x-ray residuals

1065 in QL2.P.8 in figure 7.1b do not reveal a pattern, the variation in the mean cosmics residuals
1066 do. Identifying the pattern is possible because mean cosmics residuals can be calculated
1067 across the entire area and are sensitive to smaller relative local offsets since their uncertainty
1068 is significantly smaller.

1069 The advantage of the x-ray dataset over the cosmics dataset is that absolute local offsets
1070 are measurable thanks to the reference frame provided by the alignment platforms. This is
1071 required to measure the position of strips in the ATLAS coordinate system and to satisfy the
1072 NSWs' precision tracking goals. The x-ray local offsets are being used to build an alignment
1073 model of strips in each quadruplet. It is compelling to imagine using the cosmics relative
1074 local offsets to improve the model considering their precision and ability to capture effects
1075 across the entire area of the quadruplet.

1076 **Chapter 8**

1077 **Outlook and summary**

1078 The cosmic muon dataset was used to independently confirm the local offsets measured by
1079 the x-ray method. The x-ray offsets are being used to complete the sTGC alignment scheme
1080 of the NSWs: the NSW alignment system monitors the position of alignment platforms
1081 on the surface of sTGC wedges, and the x-ray measurements provide the offsets of the strip
1082 pattern with respect to each alignment platform. The continuation of this analysis is detailed
1083 next (section 8.1) before summarizing and considering the larger context (section 8.2).

1084 **8.1 Outlook**

1085 Next all quadruplets with suitable cosmics and x-ray data should be surveyed to flag anomalous
1086 quadruplets (as a first step). If a quadruplet's correlation plot like figure 7.2 or 7.3
1087 reveals an unexpected correlation or has a large scatter, it would indicate an issue with either
1088 the cosmics or x-ray data collection to be investigated further. The uncertainty in each
1089 set of tracking points would inform the interpretation of the anomaly. Then, the quality of
1090 the correlation should be evaluated over all quadruplets instead of individually.

1091 For now, the correlation of the individual quadruplets tested support the use of the x-ray
1092 data to build an alignment model [8]. Work on creating an alignment model is ongoing.
1093 Currently, the algorithm compares the offsets of a local group of strips at each x-ray gun
1094 position as measured by the x-ray and CMM methods in a fit to extract a global slope (m)
1095 and offset (b) per layer, i , where the χ^2 is given by equation 8.1.

$$\chi^2 = \frac{[dy_{cmm,corr} - dy_{xray}]^2}{\delta dy_{xray}^2 + \delta dy_{cmm,corr}^2}, \quad (8.1)$$

$$dy_{cmm,corr} = y_{cmm} + b_i + m_i x - y_{nom} \quad (8.2)$$

1097 Here, dy is an offset as calculated from the x-ray and corrected CMM data and δdy refers
 1098 to their respective uncertainties. The CMM measurements were taken before the cathode
 1099 boards were assembled into quadruplets, so alignment parameters for the given layer were
 1100 extracted from the χ^2 fit by stepping the corrected CMM y -position towards the x-ray y -
 1101 position by adjusting the layer's slope and offset parameters. The plan is that the alignment
 1102 parameters will be provided to the ATLAS experiment's offline software to reconstruct muon
 1103 tracks from the NSWs' sTGCs. The large uncertainty on the x-ray local offsets (120 μm) and
 1104 the sparseness of the measurements means that including input from other characterization
 1105 datasets could reduce the uncertainty on the alignment model parameters.

1106 The uncertainty in the mean cosmics residuals was smaller than the desired position reso-
 1107 lution of the sTGCs, so they provide relevant information about strip positions. Moreover,
 1108 they can be calculated over the entire area of the quadruplet instead of at specific posi-
 1109 tions. It would be great to use the cosmics residuals as input to calculate and reduce the
 1110 uncertainty on the alignment parameters. Since mean cosmics residuals can only provide
 1111 relative alignment information, one idea would be to use them to constrain the fit of the
 1112 alignment parameters. In this case, the alignment parameters would need to be fitted on all
 1113 layers at once, and the shifting y -positions on each layer forced to create an abstracted track
 1114 residual equal to the local mean cosmics residual (within uncertainty) for each x-ray point.
 1115 Or, instead of constraining the fit, it could be penalized if the resulting parameters do not
 1116 result in abstracted track residuals equal to the mean cosmics residuals within uncertainty.
 1117 Some work on using the three datasets at once in a fit has been started.

1118 8.2 Summary

1119 The LHC [1] will be at the energy frontier of particle physics for at least the next decade,
 1120 making it a unique tool with which to study particle physics. With the HL-LHC [2], high
 1121 statistics on rare particle physics processes will enable more precise measurements of param-
 1122 eters of the Standard Model and increase the sensitivity to signatures of physics beyond the
 1123 Standard Model [3]. To capitalize on the increased collision rate, the NSWs of the ATLAS
 1124 experiment must be replaced to keep the triggering and tracking performance [5].
 1125 Small-strip thin gap chambers are gas ionization chambers optimized for a high rate envi-
 1126 ronment [5]. Using the pad electrodes to define a region of interest makes it possible to get
 1127 track segments of ~ 1 mrad angular resolution quickly, which will be used as input to check

1128 if a collision originated from the interaction point and should be triggered on or not [5, 53].
1129 sTGCs are also able to provide better than 100 μm position resolution on each detector plane
1130 to fulfill precision offline tracking requirements [6].

1131 Ultimately, the positions of the sTGC strip electrodes need to be known in ATLAS to within
1132 $\sim 100 \mu\text{m}$ so that they can deliver the required position resolution. The ATLAS alignment
1133 system will position alignment platforms on the surface of the sTGC wedge, and an alignment
1134 model will be used to position the strips with respect to the alignment platforms [5]. Input
1135 to the alignment model comes from the datasets used to characterize the quadruplets. The
1136 x-ray method [8] is used to measure offsets of strips from their nominal position to achieve
1137 this goal. The alignment model could be built on x-ray data alone, but the sparseness of
1138 and large uncertainty on the local offsets mean that the alignment model could benefit from
1139 more input. Comparing the x-ray offsets to the CMM data [7] allows the effect of inter-layer
1140 misalignments to be isolated and increases the input to the alignment model.

1141 The cosmics dataset was used to confirm the local offsets measured with the x-ray gun. It
1142 provides relative local offsets between sTGC strip layers. The 2D visualizations of relative
1143 local offsets allow personnel to quickly identify areas of misaligned strips and make hypothe-
1144 ses of the physical origin of those misalignments. The correlation seen between the x-ray and
1145 cosmics residuals in quadruplets with large relative misalignments confirms the validity of
1146 the x-ray local offsets. Moreover, the mean of track residuals in an area can be used to make
1147 a robust estimation of the relative local offset, as shown by the estimation of systematic
1148 uncertainties; the relative local offsets for all two-fixed layer reference frames do not change
1149 by more than 100 μm given variation in data collection conditions and analysis algorithms.
1150 The cosmics relative local offsets are therefore relevant input for alignment studies and could
1151 improve the alignment model that will position each strip.

1152 Achieving the required position resolution on each layer of the NSWs in the particle track
1153 bending plane achieves the design momentum resolution for muons ejected towards the end-
1154 caps of ATLAS. Muons are important signatures of electroweak and Higgs sector events
1155 of interest for the ATLAS Collaboration’s future physics goals [5]. Being the second of two
1156 tracking technologies on the NSWs, an effective alignment model of sTGC quadruplets layers
1157 is a necessary part of making the NSWs redundant for 10 or more years of recording collisions
1158 in the High Luminosity era of the LHC.

¹¹⁵⁹ References

- ¹¹⁶⁰ [1] L. Evans and P. Bryant. LHC Machine. *Journal of Instrumentation*, 3(S08001), August 2008.
- ¹¹⁶² [2] G. Apollinari et al. High-Luminosity Large Hadron Collider (HL-LHC) Technical Design Report V. 0.1. Technical Report CERN-2017-007-M, CERN, Geneva, September 2017.
- ¹¹⁶⁴ [3] A. Dainese et al. The physics potential of HL-LHC. In *Input to the European Particle Physics Strategy Update*, November 2018.
- ¹¹⁶⁶ [4] The ATLAS Collaboration. The ATLAS Experiment at the CERN Large Hadron Col-
¹¹⁶⁷ linder. *Journal of Instrumentation*, 3(08):S08003, August 2008.
- ¹¹⁶⁸ [5] T. Kawamoto et al. New Small Wheel Technical Design Report. Technical Report
¹¹⁶⁹ CERN-LHCC-2013-006, ATLAS-TDR-020, CERN, Geneva, June 2013.
- ¹¹⁷⁰ [6] A. Abusleme et al. Performance of a Full-Size Small-Strip Thin Gap Chamber Prototype
¹¹⁷¹ for the ATLAS New Small Wheel Muon Upgrade. *Nuclear Instruments and Methods in Physics Research Section A: Accelerators, Spectrometers, Detectors and Associated
1172 Equipment*, 817:85–92, May 2016. arXiv: 1509.06329.
- ¹¹⁷⁴ [7] E.M. Carlson. *Results of the 2018 ATLAS sTGC test beam and internal strip alignment
of sTGC detectors*. M.Sc. thesis, University of Victoria, Victoria, Canada, 2019.
- ¹¹⁷⁶ [8] B. Lefebvre. Precision survey of the readout strips of small-strip Thin Gap Chambers
¹¹⁷⁷ using X-rays for the muon spectrometer upgrade of the ATLAS experiment. *Journal of
1178 Instrumentation*, 15(07):C07013–C07013, July 2020.
- ¹¹⁷⁹ [9] D.J. Griffiths. *Introduction to elementary particles*. Physics textbook. Wiley-VCH,
¹¹⁸⁰ Weinheim, Germany, 2., rev. ed., 5. reprint edition, 2011.
- ¹¹⁸¹ [10] M.E. Peskin and D.V. Schroeder. *An introduction to quantum field theory*. Addison-
¹¹⁸² Wesley Pub. Co, Reading, Massachusetts, 1995.

- 1183 [11] P.A. Zyla et al. Review of Particle Physics. *PTEP*, 2020(8):083C01, 2020.
- 1184 [12] M. Kobayashi and T. Maskawa. CP-violation in the renormalizable theory of weak
1185 interaction. *Progress of theoretical physics*, 49(2):652–657, February 1973.
- 1186 [13] M.L. Perl et al. Evidence for Anomalous Lepton Production in $\{e\}^{\{+}\backslash ensuremath{-}\} \{e\}^{\backslash ensuremath{-}\}}$ Annihilation. *Physical Review Letters*, 35(22):1489–1492, De-
1187 cember 1975. Publisher: American Physical Society.$
- 1188 [14] F. Englert and R. Brout. Broken Symmetry and the Mass of Gauge Vector Mesons.
1189 *Physical Review Letters*, 13(9):321–323, August 1964. Publisher: American Physical
1190 Society.
- 1191 [15] P.W. Higgs. Broken symmetries, massless particles and gauge fields. *Physics Letters*,
1192 12(2):132–133, September 1964.
- 1193 [16] D. Galbraith and C. Burgard. UX: Standard Model of the Stan-
1194 dard Model, November 2013. [http://davidgalbraith.org/portfolio/
1195 ux-standard-model-of-the-standard-model/](http://davidgalbraith.org/portfolio/ux-standard-model-of-the-standard-model/) last accessed on 2021-09-30.
- 1196 [17] C.A. Bertulani. *Nuclear physics in a nutshell*. In a nutshell. Princeton University Press,
1197 Princeton, N.J, 2007. OCLC: ocm85690422.
- 1198 [18] B.W. Carroll and D.A. Ostlie. *An introduction to modern astrophysics*. Pearson
1199 Addison-Wesley, San Francisco, 2nd ed edition, 2007. OCLC: ocm69020924.
- 1200 [19] M. Boezio and E. Mocchiutti. Chemical composition of galactic cosmic rays with space
1201 experiments. *Astroparticle Physics*, 39-40:95–108, December 2012.
- 1202 [20] The SNO Collaboration. Combined analysis of all three phases of solar neutrino data
1203 from the sudbury neutrino observatory. *Phys. Rev. C*, 88:025501, August 2013.
- 1204 [21] B. Pontecorvo. Neutrino Experiments and the Problem of Conservation of Leptonic
1205 Charge. *Soviet Physics—JETP*, 53:1717–1725, 1967.
- 1206 [22] S.M. Bilenky and S.T. Petcov. Massive neutrinos and neutrino oscillations. *Reviews of
1207 Modern Physics*, 59(3):671–754, July 1987.
- 1208 [23] B. Young. A survey of dark matter and related topics in cosmology. *Frontiers of Physics*,
1209 12(2):121201, April 2017.
- 1210 [24] C. Muñoz. Dark matter detection in the light of recent experimental results. *International
1211 Journal of Modern Physics A*, 19(19):3093–3169, July 2004.
- 1212

- 1213 [25] G. Arnison et al. Experimental observation of isolated large transverse energy elec-
1214 trons with associated missing energy at s=540 GeV. *Physics Letters B*, 122(1):103–116,
1215 February 1983.
- 1216 [26] M. Banner et al. Observation of single isolated electrons of high transverse momentum
1217 in events with missing transverse energy at the CERN pp collider. *Physics Letters B*,
1218 122(5):476–485, March 1983.
- 1219 [27] G. Arnison et al. Experimental observation of lepton pairs of invariant mass around 95
1220 GeV/c² at the CERN SPS collider. *Physics Letters B*, 126(5):398–410, July 1983.
- 1221 [28] P. Bagnaia et al. Evidence for Z → e⁺e⁻ at the CERN pp collider. *Physics Letters B*,
1222 129(1):130–140, 1983.
- 1223 [29] The CDF Collaboration. Observation of Top Quark Production in $\bar{p}p$ Collisions with
1224 the Collider Detector at Fermilab. *Physical Review Letters*, 74(14):2626–2631, April
1225 1995. Publisher: American Physical Society.
- 1226 [30] The D0 Collaboration. Observation of the Top Quark. *Physical Review Letters*,
1227 74(14):2632–2637, April 1995. Publisher: American Physical Society.
- 1228 [31] The ATLAS Collaboration. Observation of a new particle in the search for the Standard
1229 Model Higgs boson with the ATLAS detector at the LHC. *Physics Letters B*, 716(1):1–
1230 29, September 2012. arXiv: 1207.7214.
- 1231 [32] The CMS Collaboration. Observation of a new boson at a mass of 125 GeV with the
1232 CMS experiment at the LHC. *Physics Letters B*, 716(1):30–61, September 2012. arXiv:
1233 1207.7235.
- 1234 [33] Standard Model Summary Plots June 2021, June 2021. <https://atlas.web.cern.ch/Atlas/GROUPS/PHYSICS/PUBNOTES/ATL-PHYS-PUB-2021-032/> last accessed on 2021-
1235 09-30.
- 1236 [34] O.S. Brüning et al. *LHC Design Report*. CERN Yellow Reports: Monographs. Geneva,
1237 2004.
- 1238 [35] ATLAS luminosity public results run-1, March 2011. <https://twiki.cern.ch/twiki/bin/view/AtlasPublic/LuminosityPublicResults> last accessed on 2021-09-20.
- 1239 [36] ATLAS luminosity public results run-2, July 2015. <https://twiki.cern.ch/twiki/bin/view/AtlasPublic/LuminosityPublicResultsRun2> last accessed on 2021-09-20.

- 1243 [37] The European Strategy for Particle Physics. Technical Report CERN/2685, CERN,
1244 2006. Adopted by the CERN council at a special session at ministerial level in Lisbon
1245 in 2006.
- 1246 [38] HiLumi HL-LHC Project. LHC/HL-LHC plan (last update january 2021). <https://hilumilhc.web.cern.ch/content/hl-lhc-project>, last accessed on 2021-09-09.
- 1248 [39] M. Cepeda et al. Report from Working Group 2: Higgs Physics at the HL-LHC and
1249 HE-LHC. *CERN Yellow Reports Monographs*, 7:221–584. 364 p, Dec 2018.
- 1250 [40] ATLAS inner detector : Technical Design Report, 1. Technical Report CERN-LHCC-
1251 97-016, CERN, April 1997. ISBN: 9789290831020 Publication Title: CERN Document
1252 Server.
- 1253 [41] S. Haywood, L. Rossi, R. Nickerson, and A. Romanouk. ATLAS inner detector :
1254 Technical Design Report, 2. Technical Report CERN-LHCC-97-017, CERN, April 1997.
1255 ISBN: 9789290831037 Publication Title: CERN Document Server.
- 1256 [42] C. Grupen, B.A. Shwartz, and H. Spieler. *Particle detectors*. Cambridge University
1257 Press, Cambridge, UK; New York, 2008. OCLC: 1105536566.
- 1258 [43] ATLAS liquid-argon calorimeter : Technical Design Report. Technical Report CERN-
1259 LHCC-96-041, CERN, 1996. ISBN: 9789290830900 Publication Title: CERN Document
1260 Server.
- 1261 [44] ATLAS tile calorimeter : Technical Design Report. Technical Report CERN-LHCC-96-
1262 042, CERN, 1996. ISBN: 9789290830917 Publication Title: CERN Document Server.
- 1263 [45] The ATLAS Collaboration. ATLAS Muon Spectrometer: Technical Design Report.
1264 Technical Report CERN-LHCC-97-022, CERN, Geneva, 1997.
- 1265 [46] ATLAS magnet system : Technical Design Report, 1. Technical Report CERN-LHCC-
1266 97-018, CERN, April 1997. ISBN: 9789290831044 Publication Title: CERN Document
1267 Server.
- 1268 [47] The ATLAS Collaboration. Performance of the ATLAS muon trigger in pp collisions
1269 at $\sqrt{s} = 8$ TeV. *The European Physical Journal C*, 75(3):120, March 2015. arXiv:
1270 1408.3179.
- 1271 [48] S. Aefsky et al. The Optical Alignment System of the ATLAS Muon Spectrometer End-
1272 caps. *Journal of Instrumentation*, 3(11):P11005–P11005, November 2008. Publisher:
1273 IOP Publishing.

- 1274 [49] ATLAS level-1 trigger : Technical Design Report. Technical Report CERN-LHCC-98-
1275 014, CERN, August 1998. ISBN: 9789290831280 Publication Title: CERN Document
1276 Server.
- 1277 [50] A. Ruiz Martínez. The run-2 ATLAS trigger system. *Journal of Physics: Conference
1278 Series*, 762:012003, October 2016.
- 1279 [51] Technical Design Report for the Phase-II Upgrade of the ATLAS TDAQ System. Tech-
1280 nical Report CERN-LHCC-2017-020, ATLAS-TDR-029, CERN, Geneva, September
1281 2017.
- 1282 [52] P. Jenni, M. Nessi, M. Nordberg, and K. Smith. ATLAS high-level trigger, data-
1283 acquisition and controls : Technical Design Report. Technical Report CERN-LHCC-
1284 2003-022, CERN, July 2003.
- 1285 [53] E. Perez Codina. Small-strip Thin Gap Chambers for the muon spectrometer upgrade of
1286 the ATLAS experiment. *Nuclear Instruments and Methods in Physics Research Section
1287 A: Accelerators, Spectrometers, Detectors and Associated Equipment*, 824:559–561, July
1288 2016.
- 1289 [54] J. Townsend. *Electricity in gases*. Clarendon Press, Oxford, 1915.
- 1290 [55] S. Majewski, G. Charpak, A. Breskin, and G. Mikenberg. A thin multiwire chamber
1291 operating in the high multiplication mode. *Nuclear Instruments and Methods*, 217:265–
1292 271, 1983.
- 1293 [56] E. Gatti, A. Longoni, H. Okuno, and P. Semenza. Optimum geometry for strip cathodes
1294 or grids in MWPC for avalanche localization along the anode wires. *Nuclear Instruments
1295 and Methods*, 163(1):83–92, July 1979.
- 1296 [57] G. Battistoni et al. Resistive cathode transparency. *Nuclear Instruments and Methods
1297 in Physics Research*, 202(3):459–464, November 1982.
- 1298 [58] B. Lefebvre. *Characterization studies of small-strip Thin Gap Chambers for the ATLAS
1299 Upgrade*. PhD thesis, McGill University, Montreal, Canada, 2018.
- 1300 [59] P.K.F. Grieder. *Cosmic rays at Earth: researcher’s reference manual and data book*.
1301 Elsevier Science Ltd, Amsterdam, 1st ed edition, 2001.
- 1302 [60] R. Keyes et al. Development and characterization of a gas system and its associated
1303 slow-control system for an ATLAS small-strip thin gap chamber testing facility. *Journal
1304 of Instrumentation*, 12(04):P04027–P04027, April 2017.

- 1305 [61] Georgios Iakovidis. VMM3, an ASIC for Micropattern Detectors. Technical Report
1306 ATL-MUON-PROC-2018-003, CERN, Geneva, March 2018.
- 1307 [62] B. Chen. *Calibration Studies of the Front-End Electronics for the ATLAS New Small*
1308 *Wheel Project*. M.Sc. thesis, McGill University, Montreal, Canada, 2019.
- 1309 [63] R. Brun and F. Rademakers. ROOT: An object oriented data analysis framework. *Nu-*
1310 *clear Instruments and Methods in Physics Research Section A: Accelerators, Spectrome-*
1311 *ters, Detectors and Associated Equipment*, 389:81–86, 1997. See also ”ROOT” [software],
1312 Release 6.18/02, 23/08/2019, (<https://zenodo.org/record/3895860#.YVJW6n0pCHs>).
- 1313 [64] F. Sauli. Principles of operation of multiwire proportional and drift chambers. In *Cern*
1314 *Yellow Reports: Monographs*, page 92 p, Geneva, 1977. CERN, CERN. CERN, Geneva,
1315 1975 - 1976.
- 1316 [65] M. Hatlo et al. Developments of mathematical software libraries for the LHC experi-
1317 ments. *IEEE Transactions on Nuclear Science*, 52:2818–2822, 2005.
- 1318 [66] H. Guo. A Simple Algorithm for Fitting a Gaussian Function [DSP Tips and Tricks].
1319 *IEEE Signal Processing Magazine*, 28(5):134–137, September 2011.
- 1320 [67] B. Stelzer. The New Small Wheel Upgrade Project of the ATLAS Experiment. *Nuclear*
1321 *and Particle Physics Proceedings*, 273-275:1160–1165, April 2016.
- 1322 [68] X. Zhao et al. Cosmic test of sTGC detector prototype made in China for ATLAS
1323 experiment upgrade. *Nuclear Instruments and Methods in Physics Research Section A:*
1324 *Accelerators, Spectrometers, Detectors and Associated Equipment*, 927:257–261, May
1325 2019.

¹³²⁶ APPENDICES

₁₃₂₇ **Appendix A**

₁₃₂₈ **Uncertainty in cluster positions**

₁₃₂₉ **A.1 Cluster definition**

₁₃₃₀ A cluster is a series of contiguous strip channels on a layer with non-zero amplitude, all
₁₃₃₁ part of the same trigger and having the same event number [58]. Clusters result from the
₁₃₃₂ drift of ionization products generate in the ionization avalanche caused by a muon [54]. The
₁₃₃₃ peak-detector-output (PDO) of the signal on each strip of a cluster is fit with a Gaussian.
₁₃₃₄ The y-position of a particle as it passed through the layer is mean of the cluster, referred to
₁₃₃₅ here as the hit position.

₁₃₃₆ **A.2 Effect of fit algorithm on cluster mean**

₁₃₃₇ The clusters were fit with Guo's method [66] and Minuit2 for ROOT [65]. The difference in
₁₃₃₈ cluster means between the two algorithms is shown in figure A.1.
₁₃₃₉ The RMS of the distribution in figure A.1 is 57 μm , which is much larger than the statistical
₁₃₄₀ uncertainty in the mean for the Minuit2 algorithm, which peaks around 7 μm . An RMS of
₁₃₄₁ 60 μm is common for data taken with most quadruplets at 3.1 kV. Therefore, the uncertainty
₁₃₄₂ in the y-hit positions is assigned 60 μm .

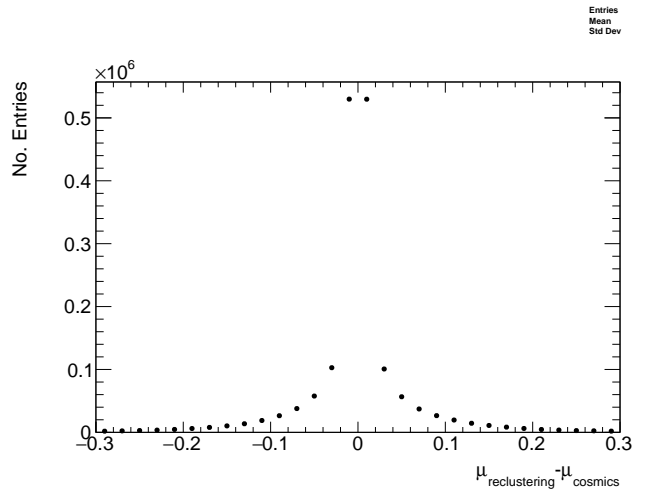


Figure A.1: The difference between cluster means calculated with Guo's method [66] in `tgc_analysis/CosmicsAnalysis` and `Minuit2` for `ROOT` [65] in `strip_position_analysis/ReClustering` for data collected with QL2.P.8 at 3.1 kV.

1343 **A.3 Effect of uncertainty in cluster mean on track residuals**

1344

1345 The uncertainty assigned to the hit position affected the uncertainty in the extrapolated/interpolated
1346 position of the track, and in the residuals. The bin size of the residual distributions was set
1347 to 200 μm because that was the uncertainty in the residuals calculated from the tracks with
1348 the least favourable geometry (like tracks built from hits on layers 1 and 2 and extrapolated
1349 to layer 4).

1350 **Appendix B**

1351 **Study of cosmics for alignment
1352 analysis statistical uncertainty**

1353 Typically, one million triggers (cosmic muon events, noise, photons and δ -rays) were collected
1354 for each Canadian quadruplet at McGill University, resulting in roughly half the number of
1355 viable tracks after cuts. For QS3.P.18, 3.5 million triggers were collected. To gauge the
1356 sensitivity of the analysis to the available statistics, partitions of this data with each with
1357 a different number of triggers were analyzed separately. Ultimately, the quantity of interest
1358 was the gaussian mean of the residual distribution in regions of interest, so the peak in the
1359 distribution of the statistical uncertainty in the residual means for each area of interest for
1360 a specific tracking combination was used to gauge the quality of the analysis. How the peak
1361 in the residual mean uncertainty distribution changes with the number of triggers is shown
1362 in figure for tracks on layer 1 built from layers 3 and 4 [B.1](#).

1363 The uncertainty is already around 20 μm at 1 million triggers, suitable for distinguishing
1364 differences in offsets of order 50 μm as required. Although increased statistics could decrease
1365 the statistical uncertainty, it is not required for the goals of this analysis. Moreoever, the
1366 systematic uncertainty is around 50 μm and the systematic uncertainty on the x-ray residuals
1367 is 150 μm so the statistical uncertainty of 20 μm is nearly negligible.

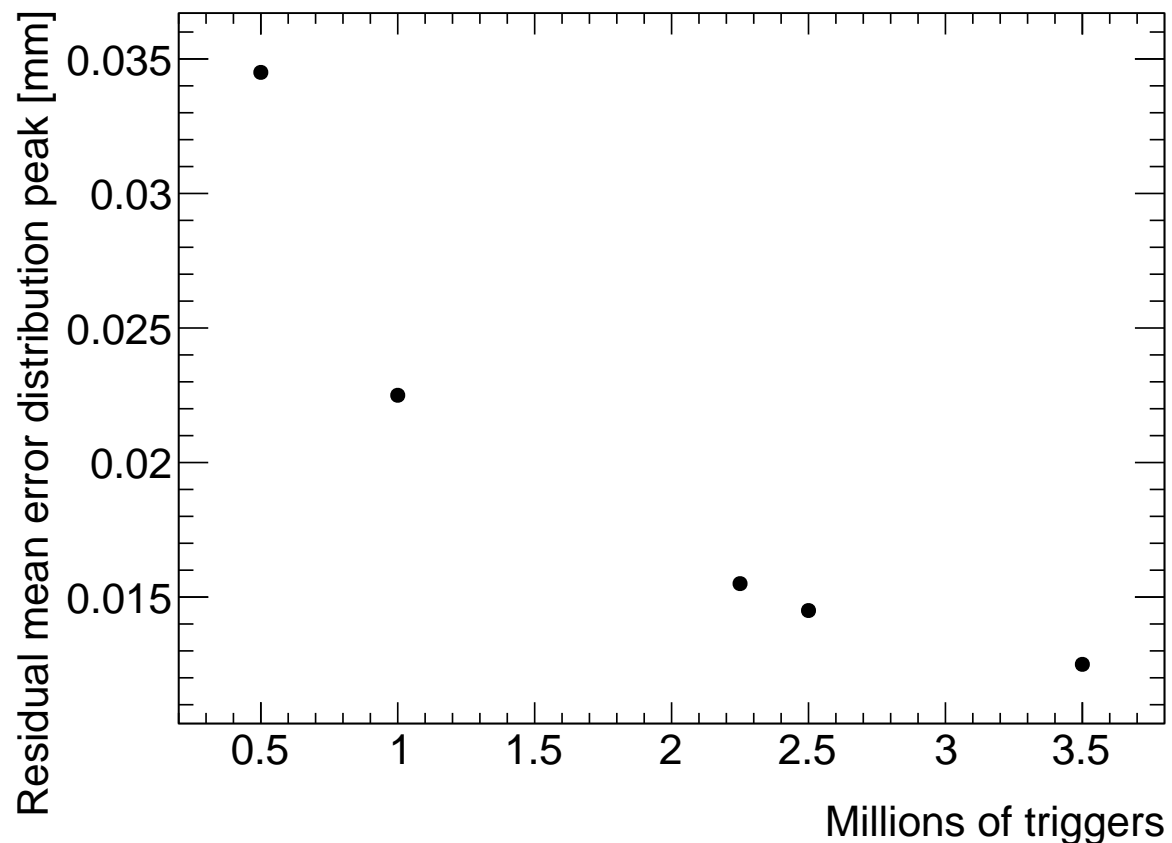


Figure B.1: How the peak of the distributions of uncertainties in the residual means in regions of interest for tracks on layer 1 built from layers 3 and 4 changed with the number of triggers used in the analysis. The distribution falls off as $\frac{1}{\sqrt{N}}$ as expected.

1368 **Appendix C**

1369 **Study of systematic uncertainties
1370 when using cosmics data for
1371 alignment studies**

1372 **C.1 Residual distribution fit function**

1373 The distribution of residuals should be modelled by a double gaussian fit[58]:

$$G(r) = A_s \exp \left[\frac{-(r - \mu)^2}{2\sigma_s^2} \right] + A_b \exp \left[\frac{-(r - \mu)^2}{2\sigma_b^2} \right] \quad (\text{C.1})$$

1374 where r is the residual, A is the gaussian amplitude, μ is the gaussian mean, σ is the
1375 gaussian sigma, and the subscripts s and b stand for signal and background respectively.
1376 One gaussian captures the real (signal) tracks and the other captures the tracks built from
1377 noise (background). The gaussian with the smaller width is identified as the signal.

1378 A single gaussian fit failed less often than a double gaussian fit. The gaussian fits were
1379 performed by initially estimating the amplitude to be 100 tracks, the gaussian mean to be
1380 the histogram mean, and gaussian σ to be the RMS. The fit range was restricted to ± 1 RMS
1381 from the histogram mean. The modification helped the gaussian fit capture the signal peak.
1382 An example residual distribution is shown in figure C.1.

1383 For all residual distributions in 100 mm by 100 mm bins on layer 4 built from hits on layers 1
1384 and 2, the difference in gaussian and double gaussian means and σ 's is shown in figure C.2.
1385 Since the RMS of the residual mean differences distribution is less than 50 μm the gaussian

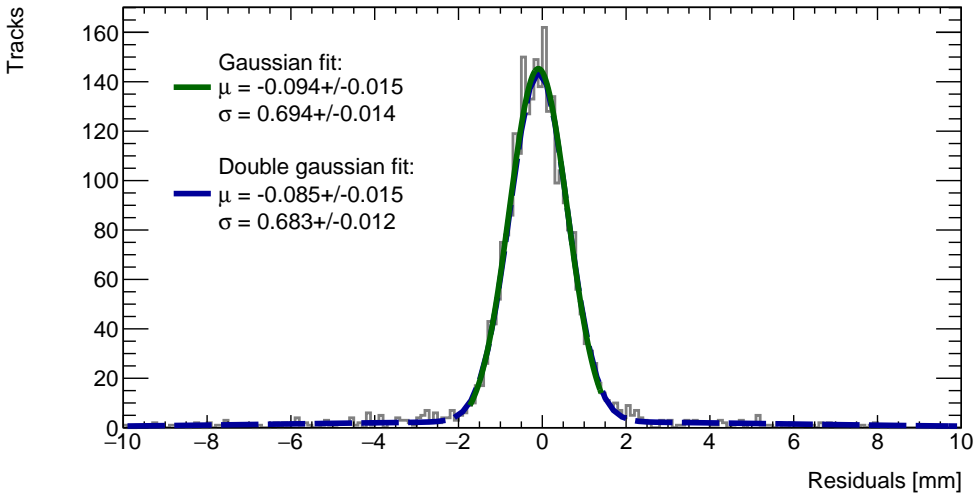


Figure C.1: Residual distribution for tracks on layer 4 built from hits on layers 1 and 2 for $x \in [-3.00, 97.00]$, $y \in [394.60, 494.60]$ mm for QL2.P.8 fit with a double gaussian and a single gaussian in a range of ± 1 RMS from the histogram mean.

1386 fit gave the same result within the required precision. Moreover, this is for the tracking
1387 combination with the worst extrapolation lever arm and the widest distribution of mean
1388 differences; the interpolation combinations have narrower distributions.

1389 The gaussian σ should be larger than the double gaussian σ because the gaussian distribution
1390 includes the effect of the noise tracks with large residuals, while the double gaussian models
1391 signal and background residuals separately. For this analysis, only the residual mean was
1392 important, so the systematic overestimate of the signal σ in the gaussian fit shown on the
1393 right of figure C.2 was allowed.

1394 C.2 Cosmic muon data collection voltage

1395 Cosmic muon data was collected at 2.9 kV and 3.1 kV because although 2.9 kV is closer to
1396 the operating conditions the chambers will be subject to in ATLAS, the extra gain provided
1397 by operating at 3.1 kV increased the signal to noise ratio for pad signals. Also, the tracking
1398 efficiency was higher with data collected at 3.1 kV. The difference in gain affected the relative
1399 population of clusters of different sizes, which in turn affected the uncertainty in the strip hit
1400 positions on each layer, the uncertainty in the track positions and the residual distributions.
1401 The residual distributions for 3.1 kV data are narrower, as shown in figure C.3.

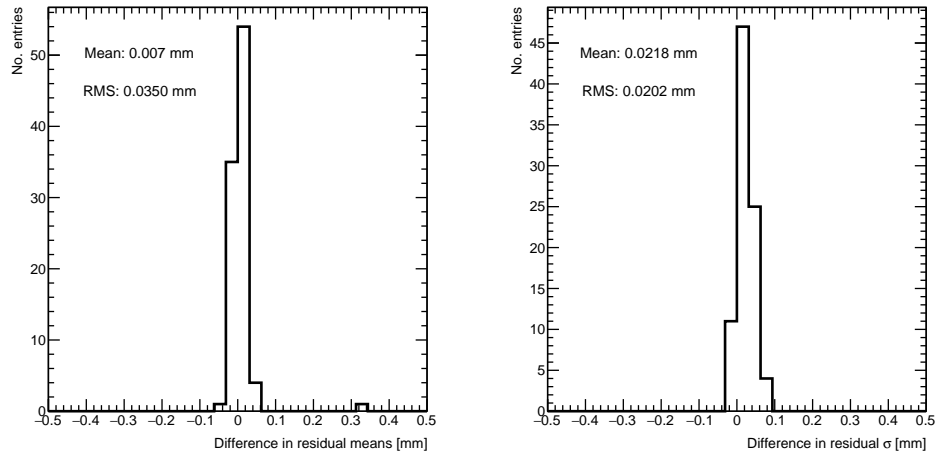


Figure C.2: Difference in residual distribution means and σ 's for a gaussian and double gaussian fit, for all residual distributions in 100 mm by 100 mm bins on layer 4 built from hits on layers 1 and 2 for QL2.P.8.

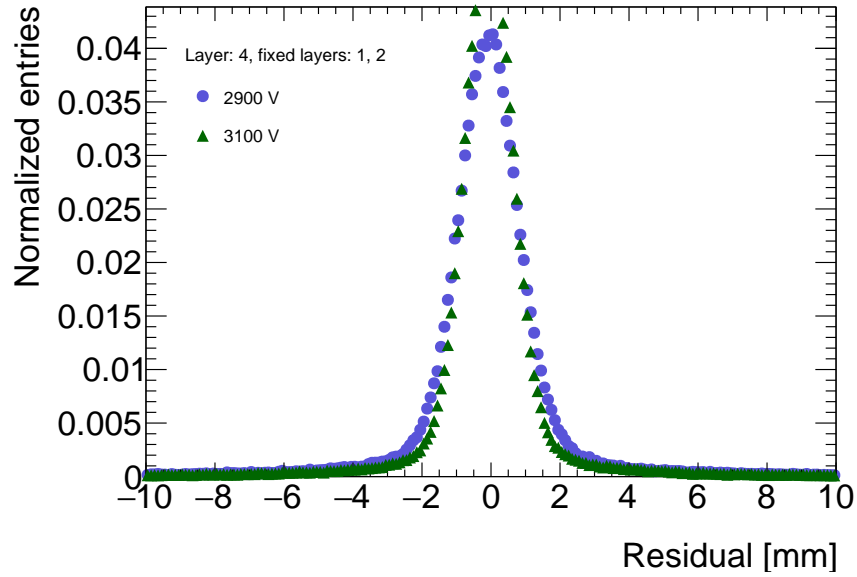
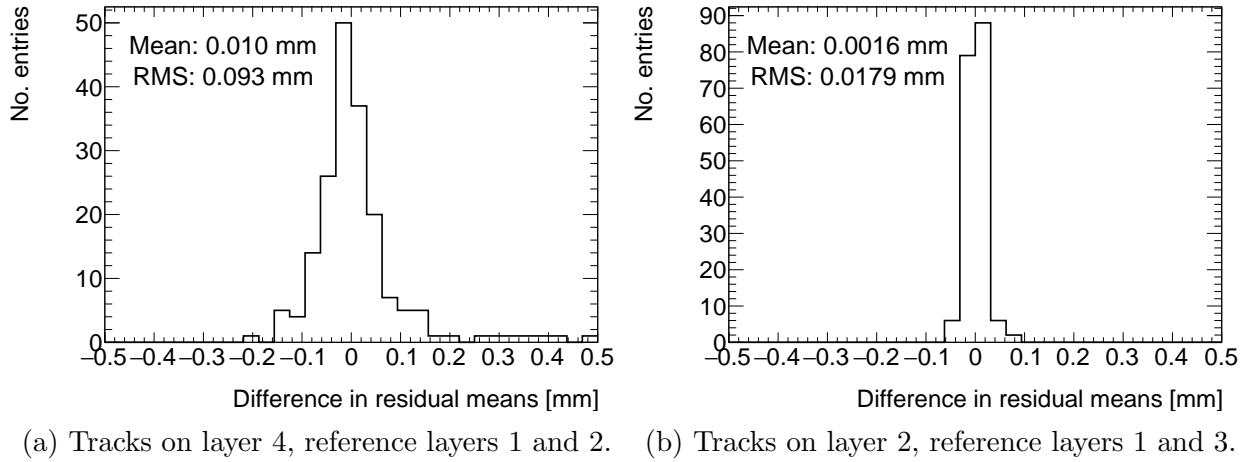


Figure C.3: Residual distribution for tracks on layer 4 built from hits on layers 1 and 2 for QL2.P.8 for data collected at 2.9 kV and 3.1 kV.



(a) Tracks on layer 4, reference layers 1 and 2. (b) Tracks on layer 2, reference layers 1 and 3.

Figure C.4: Difference in residual means for data collected with QL2.P.8 at 2.9 kV and 3.1 kV respectively in 100 mm by 100 mm bins for (a) tracks on layer 4 built from hits on layers 1 and 2 and (b) tracks on layer 2 built from hits on layers 1 and 3.

1402 Neither dataset is better for calculating the mean of residuals in a given area, so a systematic
 1403 uncertainty can be assigned based on the difference in residual means calculated for 2.9 kV
 1404 and 3.1 kV data; namely, the systematic uncertainty was approximated as the RMS of the
 1405 residual mean difference distribution. Data taken with QL2.P.8 was used to estimate the
 1406 RMS, as in figure C.4a.

1407 Tracks built from hits on layers 1 and 2 and extrapolated to layer 4 have the worst lever arm
 1408 and hence the most uncertainty. The width of the distribution for geometrically favourable
 1409 tracks are much narrower. The narrowest width of the residual mean difference distribution
 1410 is for tracks on layer 2 built from hits on layers 1 and 3 (see figure C.4b).

1411 Therefore, for each tracking combination, a systematic uncertainty equal to the RMS of the
 1412 residual mean difference distribution was assigned.

1413 C.3 Cluster fit algorithm

1414 To ensure that changing the cluster fitting algorithm like in appendix A would not change
 1415 the calculated mean of residuals in each region of interest significantly, the residual means
 1416 were compared in both cases. The distribution of the difference in residual means is plotted
 1417 in figure C.5 for the tracking combination with the worst extrapolation lever arm.

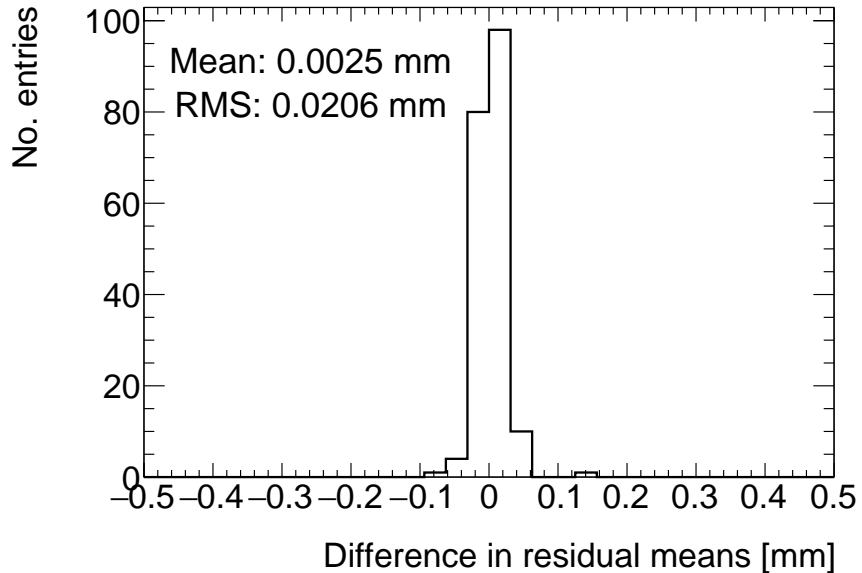


Figure C.5: Difference in residual means when the cluster fit algorithm is `Minuit2` [65] versus Guo’s method [66] for tracks on layer 4 built from hits on layers 1 and 2 for QL2.P.8.

1418 The other tracking combinations had smaller RMS values. Differences on the order of 50 μm
 1419 are important, so figure C.5 shows that the clustering algorithm had a small but notable
 1420 effect. Therefore, the RMS for each tracking combination will be used to add a systematic
 1421 uncertainty on the residual means.

1422 C.4 Differential non-linearity

1423 Definition

1424 In this context, differential non-linearity (DNL) is when the reconstructed cluster mean is
 1425 biased by the fit of the discretely sampled PDO distribution over the strips. The bias depends
 1426 on the relative position of the avalanche with respect to the center of the closest strip. For a
 1427 summary of DNL, refer to page 40 of Lefebvre’s thesis [58] and for an example application,
 1428 refer to [6].

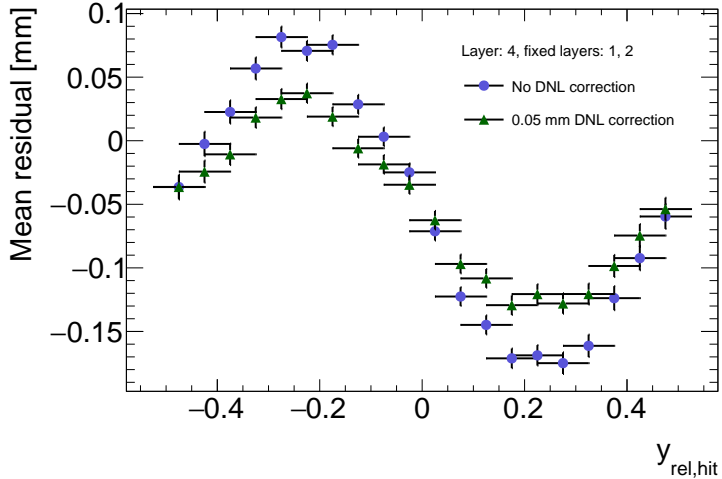


Figure C.6: Effect applying a 50 μm DNL correction to the cluster means on the residual vs y_{rel} distribution for tracks built from layers 1 and 2 and extrapolated to layer 4 for QL2.P.8.

1429 **Application and effect of DNL**

1430 The cluster mean was corrected for DNL using the equation:

$$y' = y + a \sin(2\pi y_{rel}) \quad (\text{C.2})$$

1431 where y is the cluster mean, y_{rel} is the relative position of the cluster mean with respect to
1432 the strip's center, a is the amplitude of the correction, and y' is the corrected cluster mean.
1433 The amplitude can be derived by comparing the reconstructed hit position to the expected
1434 hit position, as done in Abusleme, 2016 [6]. With cosmic muons, there is no reference hit
1435 position to compare to, so track residuals were used as a proxy [58]. The hallmark of the DNL
1436 effect is the periodic pattern in the residual versus y_{rel} profile, and the effect of correcting
1437 the cluster means using an amplitude of 50 μm is shown in figure C.6. An amplitude of
1438 50 μm was based on Lefebvre's estimate of the DNL amplitudes by layer, quadruplet and
1439 cluster size using exclusive cosmic muon tracks in `tgc_analysis/CosmicsAnalysis`. Little
1440 variation was seen in the amplitude parameters with respect to the quadruplet tested, the
1441 layer and the cluster size so a universal correction was used.

1442 Although the correction is not large enough in this case, the figure shows that the correction
1443 does reduce the DNL effect. Slightly better performance is seen in the interpolation tracking
1444 combinations where the quality of the residuals is better. DNL corrections for cosmic muon
1445 data are difficult because the DNL effect is obscured by the effect of misalignments and

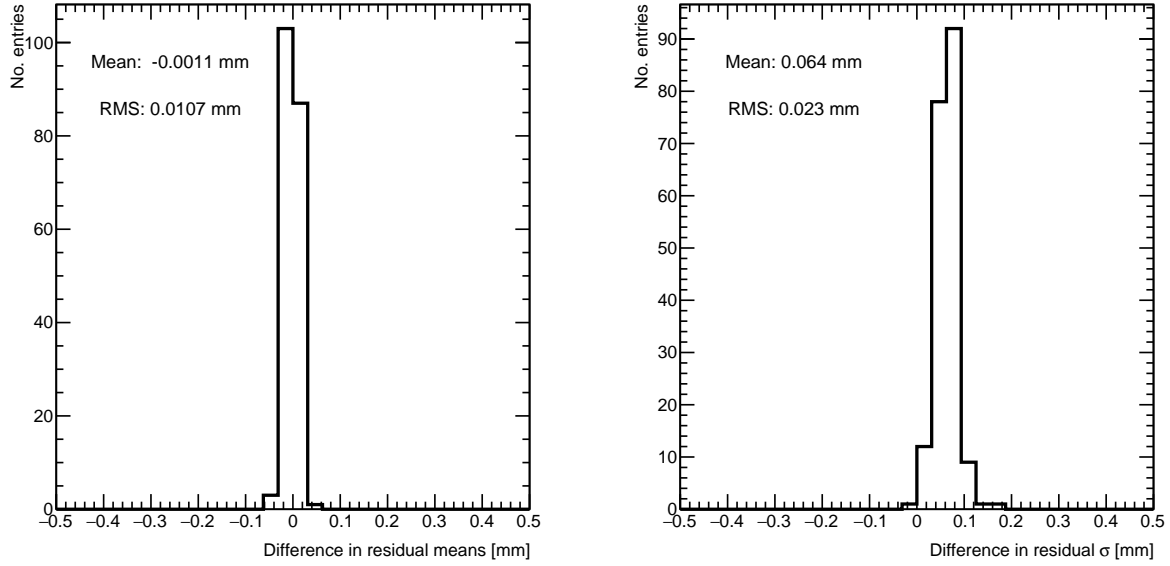


Figure C.7: Difference in residual distribution means and σ 's with and without DNL correction for residuals on layer 4 from reference layers 1 and 2 for QL2.P.8.

1446 noise. Misalignments cause the center of the sine pattern in figure C.6 to be shifted off of
1447 zero, since the mean of residuals is shifted.

1448 In figure C.7, it is apparent that the effect of the DNL correction on the mean of the
1449 residual distribution in 100 mm by 100 mm areas is on the order of micrometers in the worst
1450 extrapolation case. Although the σ 's of the residual distributions shrink with the DNL
1451 correction, the mean is the parameter of interest. Therefore, for this analysis DNL was not
1452 corrected for.

1453 The σ 's of the residual distributions do shrink with the DNL correction but not so much to
1454 affect the residual means, which are the important parameter for this analysis. Therefore,
1455 since the effect of the DNL correction is negligible, it was not pursued further.

₁₄₅₆ Appendix D

₁₄₅₇ Printable plots

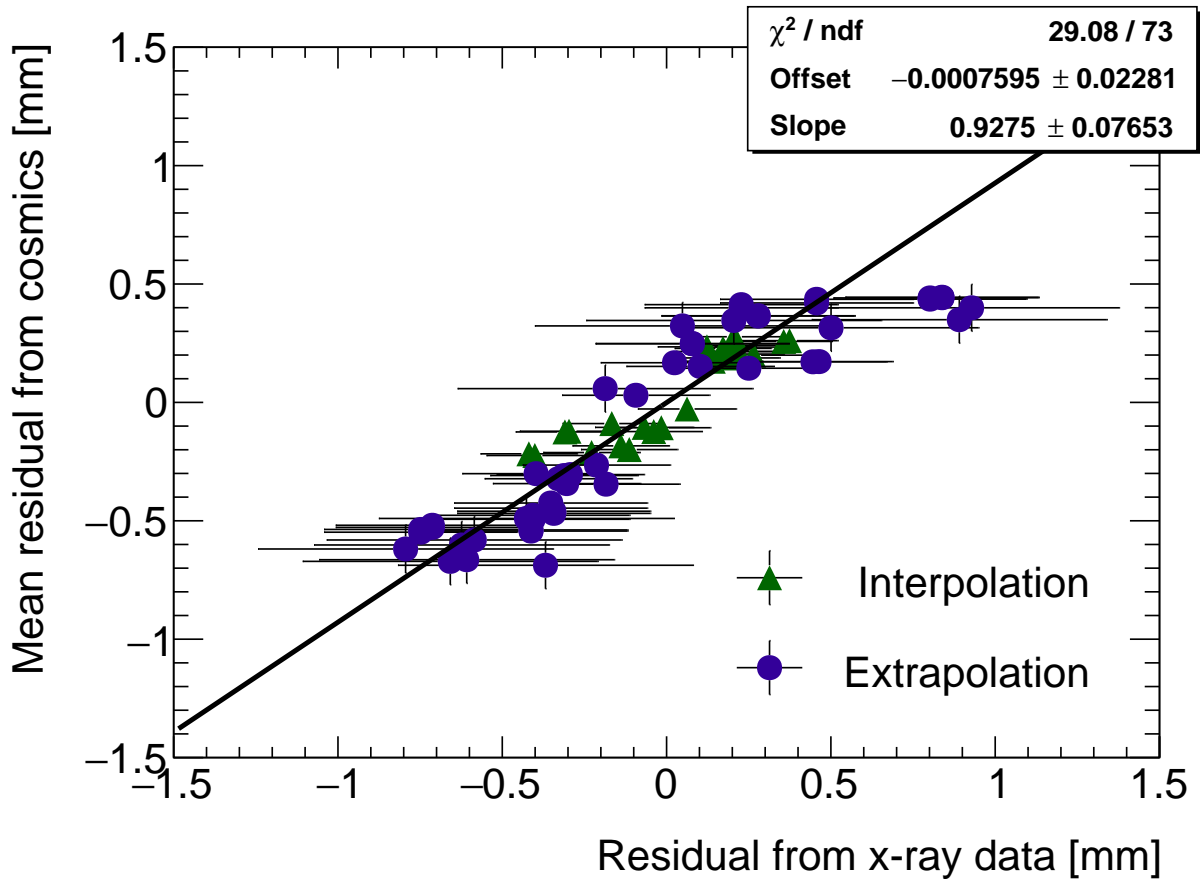


Figure D.1: Correlation plot between x-ray and cosmics residuals for all tracking combinations for QL2.P.11. Each rectangle is centered on an x-ray and mean cosmics residual pair. The width of the rectangles in x and y are the uncertainty in the x-ray and mean cosmics residual respectively. This is a printable version of figure 7.2 in section 7.1.

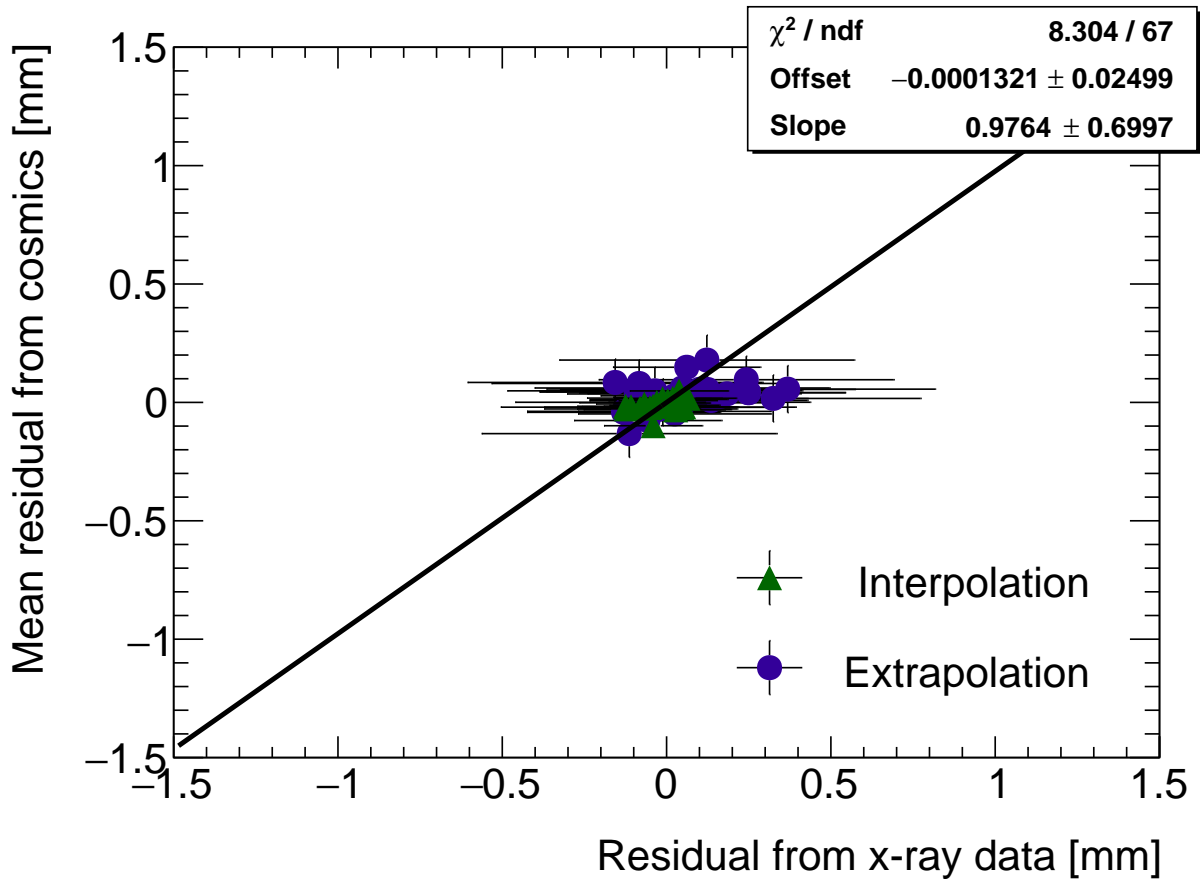


Figure D.2: Correlation plot between x-ray and cosmics residuals for all tracking combinations for QL2.P.8. Each rectangle is centered on an x-ray and mean cosmics residual pair. The width of the rectangles in x and y are the uncertainty in the x-ray and mean cosmics residual respectively. This is a printable version of figure 7.3 in section 7.1.